# Patterned apoptosis modulates local growth and tissue shape in a fast-growing epithelium

Alexis Matamoro-Vidal[1], Tom Cumming[1,2], Anđela Davidović[3] and Romain Levayer[1*§]

1. Department of Developmental and Stem Cell Biology, Institut Pasteur, CNRS UMR 3738, Université Paris Cité, 25 rue du Dr. Roux, 75015 Paris

2. PPU program Institut Pasteur, Sorbonne Université, Collège Doctoral, F75005 Paris, France

3. Department of Computational Biology, Institut Pasteur, CNRS USR 3756, 28 rue du Dr. Roux, 75015 Paris

* Correspondance to: romain.levayer@pasteur.fr

§ Lead contact

## Abstract

**What regulates organ size and shape remains one of the big mystery of modern biology. So far, this was mostly addressed by deciphering the regulation in time and space of growth and cell division, while the contribution of cell death has been much more neglected. This includes studies of the *Drosophila* wing imaginal disc, the prospective fly wing which undergoes massive growth during larval stage, one the best characterized system for the study of growth and patterning. So far, it was assumed that cell death was relatively neglectable in this tissue and as a result growth pattern is usually assimilated to the distribution of cell division. Here, using systematic mapping and registration combined with quantitative clone size/disappearance assessment, we show for the first time that cell death is not neglectable and outlined a persistent pattern of cell death and clone elimination in the disc. The local increase of cell death is associated with a significant reduction of clone size suggesting that cell death has a an impact on local growth and is not fully compensated by proliferation. Using morphometric analysis of adult wing shape and genetic perturbations, we provide evidence that patterned death affects adult wing shape. This study describes a roadmap for the proper assessment of contribution of cell death to**

**tissue shape and outlines for the first time an important instructive role of cell death in the morphogenesis of a fast growing tissue.**

**Keywords:** apoptosis, morphogenesis, growth, clone dynamics, quantitative mapping, *Drosophila*, wing imaginal disc

# Introduction

Programmed cell death and apoptosis are essential regulators of development and morphogenesis [1]. For instance, cell death is required to eliminate scaffolding tissues which are not present in the adult/larval body. Apoptosis in epithelia is also a driving force of morphogenesis which can help to fuse tissues by generating pulling forces [2] or trigger fold formations by generating apico-basal traction forces [3]. Finally apoptosis has been associated with the buffering of developmental fluctuations which can eliminate miss-specified/miss-patterned cells through cell competition [4]. Interestingly, while the functions of apoptosis are numerous, its contribution to the regulation of organ size and growth, especially in tissues undergoing fast expansion, has been poorly studied. Accordingly, emphasis has been mostly given to cellular growth regulation including the increase of cell volume and cell proliferation [5-7]. Moreover, systematic and quantitative evaluations of the pattern and number of cell deaths remain relatively rare and tedious, especially in tissue which are not appropriate for long term live imaging [8]. As such, the exact pattern of cell death and its real contribution to the regulation of organ size and shape remain poorly documented in many situations. This also applies to the *Drosophila* wing imaginal disc, one of the best studied system for the understanding of patterning and growth regulation [7, 9].

*Drosophila* wing imaginal discs are epithelial sacs composed of two apposed epithelia: the peripodal cells (lamellar epithelium) covering a pseudostratified epithelium that will from the adult structures[10]. The disc is separated in different domains that will give rise to the adult wing (the wing pouch, or wing proper) and distal region called the hinge which will connect the wing to the thorax. Wing imaginal discs undergo massive growth during larval stage through several rounds of cell division (9 to 11 cycles) [11]. This growth phase is followed by profound remodeling and morphogenesis mostly taking place during pupal stage which will lead to wing eversion, wing elongation, apposition of the two epithelial layers and formation of the final adult wing shape (**Figure 1A,B**) [12]. Decades of work have been trying to dissect the mechanism of growth and size

control of the *Drosophila* wing and have been mostly focusing on the distribution and regulation of cell proliferation while neglecting cell death [7]. Indeed, seminal works have shown more than 20 years ago that cell death is relatively minor in the wing disc and that it occurs sporadically without any noticeable pattern [13]. Yet, this did not exclude more subtle functions of cell death.

Accordingly, apoptosis was also proposed to buffer developmental fluctuations to ensure reproducible wing size [14]. This was assumed to be based on cell competition: the context dependent elimination of suboptimal cells from growing tissues[15]. Interestingly, while the studies of cell competition are mostly based on the analysis of mutant clone disappearance in the wing disc, we know virtually nothing about spontaneous clone disappearance during normal wing development and the prevalence, localization and functions of physiological cell competition.

Here, we performed a systematic mapping of apoptosis using live marker of caspases and spatial registration in the larval wing imaginal disc. Unexpectedly, we found striking reproducible biases in the distribution of cell death which outlined hot-spots of apoptosis. These hotspots correlate with a local increase of clone disappearance probability and significantly reduce local net-growth in the wing disc. Using morphometric analysis, we further demonstrate that these hot-spots can change adult wing size and shape. Altogether, we demonstrate that apoptosis cannot be neglected for the study of growth/size and is also an essential modulator of local shape and growth even in a fast expanding tissue. Our study also proposes a roadmap for a more systematic characterization of the contribution of cell death to clone dynamics and tissue growth.

# Results

### Caspase activity is spatially biased in the larval wing pouch

We first wanted to evaluate more systematically the distribution of apoptotic cells in the *Drosophila* wing disc at the larval wandering stage (96h after egg-laying). We used the live effector caspase marker GC3Ai[16] driven by a wing pouch specific driver (GMR11F02-GAL4, **Figure 1C**). The brightest GFP spots correspond to cell debris located on the basal sides, thus staining cells which already extruded (**Figure 1D**). We confirmed the accuracy of the GC3Ai marker as we obtained similar pattern with

cleaved caspase3 staining (cleaved DCP1), although the later was less sensitive and missing the less bright GC3Ai cells (**Figure 1supp E-G**). To obtain an averaged map of the distribution of cell death, we used spatial landmarks (define by the intervein marker Drosophila Serum Response Factor, DSRF) on every dissected wing disc to compute 40 sub-compartments (**Figure 1supp A-D**), and used procruste transformation (translation, rotation and scaling) to align the discs (see **Methods**). The averaged distribution of apoptotic cells revealed a striking non-homogenous distribution of apoptosis with the strongest hot spot located in the anterior and dorsal compartment near the dorso-ventral boundary (**Figure 1 F,G**). This bias is not driven by the driver or some side effect of GC3Ai as a similar pattern was obtained in the *w*⁻ background with cleaved caspase3 staining (**Figure 1supp H-J**), or with GC3Ai driven by another wing pouch driver (*nubbin-gal4*, **Figure 1supp K**). To check whether this bias persists during wing disc development, we also detected GC3Ai positive cells in early L3 wing disc (72h after egg-laying). While we could not use the same spatial landmarks (the intervein region are not yet defined at this stage) we used instead the localisation of the 4 compartments defined by AP and DV compartment boundaries (Anterior, Posterior, Dorsal and Ventral). There was more than a two folds increase of the number of apoptotic cells in the anterior-dorsal compartment compared to the others (**Figure 1 J-L**). This suggested that the spatial bias emerges at least during early L3 stage and persists for more than 24 hours. We then checked whether this pattern was indeed caspase dependent. Co-expression of GC3Ai with a dominant negative of Dronc (*Drosophila* caspase 9) significantly reduced the number of GC3Ai dots and abolished the spatial bias (**Figure 1H**, **Figure 1supp O-Q**). Similarly, depletion of the pro-apoptotic gene *hid* by RNAi in the wing pouch almost completely abolished the GC3Ai signal (**Figure 1I**, **Figure 1supp L-N**). This suggests that the spatial bias is indeed caspase dependent and most likely relies on the expression of the pro-apoptotic gene *hid*. Accordingly, we found a slight but systematic and reproducible increase of *hid* expression near the GC3Ai hot spot region using a GFP insertion at the *hid* locus (**Figure 1M,N**). Note however that other factors may also contribute to the spatial bias as we still observed some heterogeneity in cell death distribution upon Dronc inhibition or *hid* depletion (**Figure 1supp R,S**).

Altogether, we concluded that contrary to what was previously suggested[13], apoptosis is not homogeneous in the wing imaginal disc and that some regions

(anterior and close to the DV boundary, dorsal compartment) undergo higher rates of apoptosis. These hotspots are partially explained by spatial bias in the expression of the pro-apoptotic gene *hid*.

**The spatial bias in caspase activity increases locally clonal disappearance and reduces local net-growth.**

We then checked whether this spatial bias in apoptosis could have any consequence on clonal dynamics and local growth. Since ex-vivo live imaging of wing disc does not allow long term tracking of cell fate and local growth, we used an alternative approach based on twin-clone labelling. We first used the QMARCM technic [17] to stain the two daughter cells generated after mitotic recombination with different fluorescent markers and express different set of transcription factors (Gal4 or the Qsystem, **Figure 2A,B**). We assessed the probability of clone disappearance by scoring the number of single-coloured clone which are not in vicinity of the other sibling clone 48h after clone induction (which can only be explained by the early disappearance of the lineage of the other daughter cell). We noted first that the QMARCM system has an intrinsic bias with smaller clones and higher probability of clone disappearance for GFP/Gal4 clones (**Figure 2suppA**). This however should not preclude the analysis of potential spatial biases. By multiplexing a large number of discs and using the same spatial landmarks as the one used in **Figure 1suppC** (**Figure 2B**), we could obtain a coarse-grained map of the probability of clone disappearance (**Figure 2C**). Strikingly, we observed once again that the probability of clone disappearance is not spatially homogenous and identified clear hotspots of clone death, including the anterior-dorsal region near the DV boundary (~2 fold increase compared to posterior compartments at similar DV positions, **Figure 2C, 2suppB**), as already outlined by the caspase positive cells mapping (**Figure 1G**). Note that this clone strategy reflects apoptosis pattern at earlier stages of development compared to the one revealed with GC3Ai. A similar bias could be outlined by an alternative twin-clone method (twin spot MARCM[18], using RNAi depletion of RFP and GFP with Gal4 expressed in the wing pouch, **Figure 2D, 2suppB**) suggesting that the spatial bias is not specific of the clone induction system. Importantly, clone size was also on average smaller (estimated either through total surface or number of cells) in regions showing high rates of apoptosis and clone disappearance (**Figure 3A, Figure 3suppA-C,E**). This suggested that spatial biases in caspase activity not only modulate the probability of clone survival, but also the

cumulated local growth in the wing disc. Indeed, the local differences in clone size match the differences numerically estimated from an exponential growth model with no spatial difference in proliferation rate, and including spatial differences in apoptotic rates estimated from our measurements of clone disappearance (see **Methods, Figure 3B-D**), suggesting that local differences in clone size could be solely explained by spatial differences in apoptotic rates. To check whether these spatial differences are indeed driven by caspases, we used the QMARCM clonal assay upon inhibition of caspase in the Gal4 sibling clones (using UAS-Dronc$^{DN}$). While this did not totally abolish clone disappearance, the pattern was flattened with no visible hotspot of clone disappearance in the anterior side (**Figure 2C', 2suppB**). A similar effect was obtained upon global inhibition of *hid* in the wing pouch by RNAi with the twin-spot MARCM assay (**Figure 2D', 2suppB**). These two approaches also flattened the inhomogeneity of clone size between anterior and posterior compartments in the wing disc (**Figure 3supp D,F**).

Altogether, we concluded that the spatial bias in *hid* expression and caspase activity generate a hotspot of clone disappearance which also reduces significantly local growth rate mostly in the dorsal-anterior region near the DV boundary. This suggested that local increases of caspase activity could play an instructive role which significantly modulates local growth, which therefore may affect the final shape of the tissue.

**Patterned caspase activity modulates adult wing shape and size**

We therefore checked whether local biases in caspase activity could significantly impact adult wing shape and size. To obtain a precise and quantitative description of adult wing shape, we used a quantitative assay based on semi-automatic wing segmentation, landmark positioning and procruste alignment of wings (which includes translation, rotation and global rescaling)[19, 20] (**Figure 4supp A**). Interestingly, inhibition of cell death in the wing pouch using *hid* RNAi led to a significant increase of wing size (**Figure 4B,** 5.5%, a similar range to what is obtained upon ectopic overexpression of Dp110/PI3K[21]), suggesting that apoptosis has a net negative effect on adult tissue size. We also observed significant changes of adult wing shape, including a global increase of the size of the most anterior and posterior domains, as well as a global wing rounding (**Figure 4C,E,F**). To check whether local increases of apoptosis were indeed responsible for the local modulation of shape and size, we used various drivers to inhibit apoptosis in different wing subdomains (**Figure 4A**).

Accordingly, inhibition of *hid* in the patched domain (*ptc-gal4*, expressed in a band near the AP compartment boundary, **Figure 4A**) led to a global increase of wing size dominated by the expansion of the region overlapping the *ptc* domain (**Figure 4B,C**). This suggested that apoptosis has a local impact on growth even in region outside the apoptosis hotspots identified at larval stage. We also used drivers restricted to the DV boundary either in the anterior (encompassing the caspase hotspot, **Figure 1G**) or posterior part of the wing disc (**Figure 4A**). Interestingly, while *hid* depletion in the posterior-DV boundary domain had a mild effect on wing size (similar to inhibition of *hid* in the ptc domain), this effect was much more significant upon inhibition in the anterior-DV boundary domain reaching differences close the one observed upon inhibition of *hid* in the full wing pouch (4.1% versus 5.5% increase, **Figure 4B**). This suggests that apoptosis around the anterior DV margin (the strongest hotspot of apoptosis) can account for a good proportion of the effect on adult wing size. Importantly, the expansion of the most anterior domain of the wing was only observed upon inhibition of *hid* in the anterior-DV boundary domain (**Figure 4C**), suggesting again that apoptosis has a local effect on size. We also performed experiments with conditional *hid* depletion to assess the relative contribution of *hid* expression at larval stage versus pupal stage to the final wing shape. While depletion of *hid* at mid-early pupal stage only had a minor effect on wing shape (**Figure 4D-F, 4supp E**), *hid* depletion from early larval stage to early pupal stage was sufficient to recapitulate the rounding of the wing and the main shape modulation observed upon *hid* depletion throughout development (**Figure 4D-F, 4suppE)**. Note that we could not use this context to analyze the effect on absolute size, as it was completely dominated by the well documented effect of temperature on wing size[22, 23] (**Figure 4suppD**). To have a more quantitative description of shape changes induced by these genetic backgrounds, we used Principal Components Analysis applied to the 48 landmarks defined by the wing segmentation (**Figure 4suppA**). The combinatorial effect of *hid* depletion during larval and pupal stage is well reflected by this PCA analysis (**Figure 4D**), which can decompose the effect of *hid* depletion throughout development ("full expression", purple arrow) in the sum of a strong effect coming from the larval stage along Principal Component 1 ("early expression", blue arrow, along PC1) and a mild effect related to the depletion during pupal stage ("late expression", green arrow, mild effect along PC2). Accordingly, PC1 mostly reflects the rounding of the wing (**Figure 4E**, accounting for 61% of the variation in the PCA analysis) while PC2 mostly relies

on the shift of the posterior cross-vein (**Figure 4E**, accounting for 13% of the variation of the PCA analysis). The effect of this temporal depletion, combined with the wing pouch specificity of the other drivers strongly argue for the important role of *hid* pattern of expression in the pouch during larval development.

Altogether, we conclude that spatial biases in apoptosis distribution in the growing wing disc can significantly modify the shape of the adult wing by locally reducing net growth. This suggests that the fine spatial tuning of apoptosis in a fast-growing tissue plays an instructive role for organ shape and size regulation.

## Discussion

In this study, we outlined an unexpected pattern of apoptosis in the growing wing imaginal disc with a significant upregulation in the anterior and dorsal compartment of the wing. This is to our knowledge the first demonstration that apoptosis is spatially biased in the wing imaginal disc. Moreover, our quantitative assessments of clonal growth and adult wing shape clearly show that this local upregulation of apoptosis has a significant impact on local net growth and final adult shape. So far, the characterization of cell death was never performed in a systematic manner using spatial landmarks, which may explain why such biases have been missed[13]. Similarly, the impact of apoptosis on wing adult shape and size has never been studied with such quantitative readouts. More generally, the assessment of apoptosis levels and distributions is usually based on cleaved caspase3 and Tunnel staining [8]. However, in conditions where the lifetime of apoptotic debris is relatively short, these assays may easily miss potential pattern of interest and may underestimate the real contribution of apoptosis. Our work strongly argues for the need of more systematic quantitative assessments of death distribution prior to conclude anything about the contribution of apoptosis to organ shape/size regulation. The pipeline we used in this study may easily be applied in other developmental contexts which are not amenable for long term live imaging, as long as markers can be used for spatial registration and tools are available for clone generation.

Compensatory proliferation is one of the best studied process that relates apoptosis to the induction of cell proliferation[24]. So far, this process was mostly characterized either in conditions of massive death induction through irradiation and genetic induction of apoptosis in large domains[25, 26], or through the perturbation of the core apoptotic

pathway (e.g.: by blocking some of the essential caspases, caspase3 in *Drosophila*[27], or caspase9 in mammalian epidermis[28]). However, to our knowledge there is no study that clearly identified biases in cell proliferation distribution in vicinity of physiological apoptosis *in vivo*. Surprisingly, we observed a net negative effect of the local increase of cell death on local growth and the size of the final adult compartment, and also outlined a significant effect of physiological death on the final size of the adult wing (**Figure 2** and **Figure 4**). This suggests that compensatory proliferation is unlikely to occur in the context of physiological apoptosis, or at least that its contribution is relatively minor and not sufficient to compensate for the loss of cell by apoptosis. Further work studying quantitatively the coupling between apoptosis and cell proliferation would be essential to assess its real contribution to physiological growth regulation. Interestingly, a recent study outlined a significant positive upregulation of proliferation near dying cell in MDCK cell, however this effect is strongly context dependent and is not visible at low stiffness or high density values[29], conditions that may apply to the wing imaginal disc.

Cell competition is the process describing the context dependent elimination of viable but suboptimal cells[4]. Studies of clonal elimination in the wing imaginal disc have largely contributed to our understanding of this process. Interestingly, most of these studies assumed that clone disappearance in physiological conditions is largely neglectable. Our results suggest that a significant proportion of WT clones may undergo early elimination in the wing imaginal disc, and that this elimination is spatially biased. On the one hand, this opens the possibility for spontaneous competition occurring in the wing imaginal disc, which so far has never been explored thoroughly (although indirect genetic evidence suggested there might be[14, 30]). On the other hand, it also suggests that cell elimination during competition may be influenced by this spatial pattern of caspase activity and apoptosis. Further quantitative description of clonal elimination during competition may reveal such spatial bias and would help to study the influence of pre-existing pattern of caspases/apoptosis on cell competition and tissue plasticity.

In this study, we showed that local modulation of *hid* expression can fine-tune the local level of apoptosis which will impact local growth and adult tissue shape. As such, the evolution of the cis-regulatory elements of pro-apoptotic genes may be an additional leverage of shape evolution that could be used to fine tune appendage adult shape.

Interestingly, these pro-apoptotic genes are most likely less pleiotropic than pro-proliferative pathways such as morphogens, RTK signaling pathways, or Hippo pathways that are classically studied for the regulation of size and growth[7]. As such, modulating pro-apoptotic genes levels and pattern of expression may constitute a relatively parsimonious way to evolve wing and appendage shape.


## Acknowledgements

We thank members of RL lab for critical reading of the manuscript. We would like to thank Christina Fissoun, Lucia Rodriguez Vazquez, Gaurav Shajepal and Delia Cicciarello for their contribution to adult wing and wing disc analysis during their internship. We are also grateful to Jean-Paul Vincent, Magalie Suzanne, David Houle, Seth Blair, the Bloomington Drosophila Stock Center, the Drosophila Genetic Resource Center and the Vienna Drosophila Resource Center, Flybase for sharing essential information, stocks and reagents. We also thank Benoît Aigouy for the Packing Analyser software and Jean-Yves Tinevez and the image analysis platform of Institut Pasteur for the localProjection plugin on Fiji. Work in RL lab is supported by the Institut Pasteur (G5 starting package), the ERC starting grant CoSpaDD (Competition for Space in Development and Disease, grant number 758457), the Cercle FSER and the CNRS (UMR 3738).


## Authors contribution

RL and AMV discussed and designed the project and wrote the manuscript. TC performed part of the experiments on adult wing shape and twin clones analysis as well as the wing disc segmentation. AD provided the theoretical calculation of the expected distribution of clone size based on differences in apoptotic rates. AMV performed all the other experiments and analysis. Every author has commented and edited the manuscript.

## Declaration of interests

The authors declare no competing interest

# Methods

### Ressource availability

*Lead contact*

Further information and requests for resources and reagents should be directed to and will be fulfilled by the lead contact, Romain Levayer (romain.levayer@pasteur.fr).

*Material availability*

All the reagents generated in this study will be shared upon request to the lead contact without any restrictions.

*Data and Code availability*

All code generated in this study and the raw data corresponding to each figure panel (including images and local projection of movies) can be shared upon request and will be uploaded soon to a repository.

**Experimental model and subject details**

*Drosophila melanogaster husbandry*

All the experiments were performed with *Drosophila melanogaster* fly lines with regular husbandry technics. The fly food used contains agar agar (7.6 g/l), saccharose (53 g/l) dry yeast (48 g/l), maize flour (38.4 g/l), propionic acid (3.8 ml/l), Nipagin 10% (23.9 ml/l) all mixed in one liter of distilled water. Flies were raised at 25°C in plastic vials with a 12h/12h dark light cycle at 60% of moisture unless specified in the legends and in the table below (alternatively raised at 18°C or 29°C). Females and males were used without distinction for all the experiments. We did not determine the health/immune status of pupae, adults, embryos and larvae, they were not involved in previous procedures, and they were all drug and test naïve.

*Drosophila melanogaster strains*

The strains used in this study and their origin are listed in the table below.

| Fly line | Chromosome location | Origin (citation) | RRID |
|---|---|---|---|
| *UAS-GC3Ai /TM6b* | III | [16], Magalie Suzanne | none |
| *w; UAS-GC3Ai/Cyo ; MKRS/TM6b* | II | Bloomington and [16] | BDCS_84346 |
| *UAS-hid dsRNA* | III | VDRC | GD 8269 |

| | | | |
|---|---|---|---|
| *UAS-lacZ* | II | Bloomington | BDCS_8529 |
| *UAS-dronc$^{DN}$* | II | Boomington | BDCS_58992 |
| *GMR11F02-gal4* | III | Bloomington | BDCS_48928 |
| *w$^{118}$* | X | Bloomington | BDCS_3605 |
| *UAS-dicer2 ; nubbin-gal4* | X, II | Bloomington | BDCS_25754 |
| *w; ; hid$^{\Delta.GFP}$/TM3* | III | [31], Jean-Paul Vincent | none |
| *yw; ET40-QF, QUAS-tdTomato; FRT82B, tub-QS* | X, II, III | Bloomington | BDCS_30042 |
| *yw, hs-flp22, UAS-GFP ; if/Cyo ; tub-gal4, FRT82B, tub-gal80/TM6b* | X, III | This study and Bloomington | BDCS_86311 |
| *yw; UAS-mCd2RFP , UAS-dsRNACD8 FRT40A ; TM3/TM6b* | II, III | Bloomington | BDCS_56184 |
| *yw; UAS-mcd8GFP, UAS-dsRNACD2 FRT40A ; TM3/TM6b* | II, III | Bloomington | BDCS_56185 |
| *w; ptc-gal4* | II | Bloomington | BDCS_2017 |
| *w; GMR83F09-gal4* | II | Bloomington | BDCS_40367 |
| *w; GMR36C06-gal4* | II | Bloomington | BDCS_49931 |
| *w; tub-gal80ts* | II | Bloomington | BDCS_7108 |
| *w; UAS-lacZ* | II | Bloomington | BDCS_8529 |

The exact genotype used for each experiment is listed in the next table. AEL: hours after egg laying, hs : heat shock duration at 37°C, ACI : time after clone induction.

| **Figure** | **Genotype** | **Clone induction** | **Dev. time** |
|---|---|---|---|
| 1 A-G, J-L | *w; + ; GMR11F02-gal4/UAS-GC3Ai* | - | 96h AEL |
| 1 H | *w; UAS-dronc$^{DN}$/+ ; GMR11F02-gal4/UAS-GC3Ai* | - | 96h AEL |
| 1 I | *w; UAS-GC3Ai/+ ; GMR11F02-gal4/ UAS-hid-dsRNA* | - | 96h AEL |
| 1 J-L | *w; + ; GMR-11F02-gal4/UAS-GC3Ai* | - | 72h AEL |
| 1 M,N | *w ; + ; hid$^{\Delta GFP}$/TM3* | - | 96h AEL |
| 1supp A-G, R,S | *w; + ; GMR11F02-gal4/UAS-GC3Ai* | - | 96h AEL |
| 1supp H-J | *w$^{118}$* | - | 96h AEL |
| 1supp K | *UAS-dicer2; nubbin-gal4/+ ; UAS-GC3Ai/+* | - | 96h AEL |
| 1supp L-N, R,S | *w; UAS-GC3Ai/+ ; GMR11F02-gal4/UAS-hid-dsRNA* | - | 96h AEL |
| 1supp O-Q,R,S | *w; UAS-dronc$^{DN}$/+ ; GMR11F02-gal4/UAS-GC3Ai* | - | 96h AEL |
| 2B, 2C, 2suppA,B | *yw hs-flp22, UAS-GFP/+; ET40-QF, QUAS-tdTomato/Cyo-If; FRT82B, tub-QS/FRT82B, tub-gal80* | 8 min hs, 48h ACI | 96h AEL |
| 2C', 2supp A,B | *yw hs-flp22, UAS-GFP/+: UAS-dronc$^{DN}$/ET40-QF, QUAS-tdTomato; FRT82B, tub-QS/FRT82B, tub-gal80* | 8 min hs, 48h ACI | 96h AEL |
| 2D, 2supp A,B | *yw hs-flp22; UAS-mCd2RFP , UAS-dsRNACD8 FRT40A/UAS-mcd8GFP, UAS-dsRNACD2, FRT40A; GMR11F02-gal4/+* | 10 min hs, 48h ACI | 96h AEL |

| | | | |
|---|---|---|---|
| 2D', 2supp A,B | *yw hs-flp22; UAS-mCd2RFP , UAS-dsRNACD8 FRT40A/UAS-mcd8GFP, UAS-dsRNACD2, FRT40A; UAS-hid dsRNA/GMR11F02-gal4* | 10 min hs, 48h ACI | 96h AEL |
| 3A-D | *yw hs-flp22, UAS-GFP/+; ET40-QF, QUAS-tdTomato/Cyo-If; FRT82B, tub-QS/FRT82B, tub-gal80* | 8 min hs, 48h ACI | 96h AEL |
| 3supp A-C | *yw hs-flp22, UAS-GFP/+; ET40-QF, QUAS-tdTomato/Cyo-If; FRT82B, tub-QS/FRT82B, tub-gal80* | 8 min hs, 48h ACI | 96h AEL |
| 3supp D | *yw hs-flp22, UAS-GFP/+; UAS-dronc$^{DN}$/ET40-QF, QUAS-tdTomato; FRT82B, tub-QS/FRT82B, tub-gal80* | 8 min hs, 48h ACI | 96h AEL |
| 3supp E | *yw hs-flp22; UAS-mCd2RFP , UAS-dsRNACD8 FRT40A/UAS-mcd8GFP, UAS-dsRNACD2, FRT40A; GMR11F02-gal4/+* | 10 min hs, 48h ACI | 96h AEL |
| 3supp F | *yw hs-flp22; UAS-mCd2RFP , UAS-dsRNACD8 FRT40A/UAS-mcd8GFP, UAS-dsRNACD2, FRT40A; UAS-hid dsRNA/GMR11F02-gal4* | 10 min hs, 48h ACI | 96h AEL |
| 4A | *yw; UAS-mCd2RFP,UAS-dsRNACd8 FRT40A ; GMRF1102-gal4/TM3* | - | 96h AEL |
| 4A | *w; UAS-lacZ/aristaless-gal4* | - | 96h AEL |
| 4A | *w; UAS-lacZ/trithorax-gal4* | - | 96h AEL |
| 4A | *w; UAS-lacZ/ptc-gal4* | - | 96h AEL |
| 4B-C | *w; UAS-lacZ/+; GMRF11F02-gal4/+* | - | adult |
| 4B-C | *w; +; GMRF11F02-gal4/UAS-hid dsRNA* | - | adult |
| 4B-C | *w; UAS-lacZ/aristaless-gal4; +* | - | adult |
| 4B-C | *w; aristaless-gal4/+; UAS-hid dsRNA/+* | - | adult |
| 4B-C | *w; UAS-lacZ/trithorax-gal4; +* | - | adult |
| 4B-C | *w; trithorax-gal4/+; UAS-hid dsRNA/+* | - | adult |
| 4B-C | *w; UAS-lacZ/ptc-gal4 ; +* | - | adult |
| 4B-C | *w; ptc-gal4/+ ; UAs-hid dsRNA/+* | - | adult |
| 4D-F | *w; UAS-lacZ/tub-gal80$^{ts}$; GMRF11F02-gal4/+* | - | adult |
| 4D-F | *w; +/tub-gal80$^{ts}$; GMRF11F02-gal4/UAS-hid dsRNA* | - | adult |
| 4supp A | *w$^{118}$* | - | adult |
| 4supp D-E | *w; UAS-lacZ/tub-gal80$^{ts}$; GMRF11F02-gal4/+* | - | adult |
| 4supp D-E | *w; +/tub-gal80$^{ts}$; GMRF11F02-gal4/UAS-hid dsRNA* | - | adult |

**Immunostaining**

Dissections of larval wing imaginal discs were performed on PBS in ice. Dissected discs were fixed for 20 min in 4 % formaldehyde (SIGMA F8775), rinsed 3 times in PBT (PBS 0.4 % Triton), followed by 10 min permeabilisation in PBT. Primary and secondary antibodies were incubated for 2 h at room temperature (or 12 h at 4 °C) under rocking agitation. After each antibody incubation, discs were rinsed 3 times in PBT, followed by 3 washes of 30 min. Discs were mounted in Vectashield® (EUROBIO SCIENTIFIC / H-1000) and imaged using a confocal spinning disc microscope (Gataca systems) with a 40X oil objective or a LSM880 equipped with a fast Airyscan using a 40X oil objective. The following primary antibody were used: rat anti E-cadherin (1/100, DCAD2 concentrated DSHB), mouse anti DSRF (1/500, gift of Seth Blair), rat anti Delta

(1/1000, gift of François Schweisguth), chicken anti GFP (1/1000, abcam ab13970), rabbit anti RFP (1/500,), rabbit anti DCP-1 (1/100, Cell Signaling 9578S), chicken anti Beta-gal (1/1000, Abcam ab 9361), mouse anti Wingless (1/250, 4D4 concentrated DSHB), mouse anti Patched (1/250, Apa-1 concentrated, DSHB), phalloidin alexa 647 (1/50, Invitrogen). Secondary antibodies were: anti rabbit alexa 555 (1/500, Invitrogen), anti chicken alexa 488 (1/500, Invitrogen), ultrapurified anti mouse 405 (1/500, Jackson ImmunoResearch / 715-476-151), ultrapurified anti mouse CY3 (1/500, Jackson ImmunoResearch / 715-165-151), ultrapurified anti rat 647 (1/500, Jackson ImmunoResearch / 712-605-153).

**Image processing**

All images were processed using FIJI[32] . For the twin clones analyses, Z projections of z-stacks were done using the Fiji LocalZprojector plugin using E-cad or phalloidin staining as a reference plane[33], allowing to project a limited number of planes around the apical junction plane while following the local disc curvature. *hid*$^{\Delta GFP}$ pattern measurement were done after fixation and GFP immunostaining and maximum z projection. The mean GFP intensity was measured in each compartment (defined with DSRF staining) and normalised by the mean GFP intensity of the full wing pouch.

**QMARCM and twin spot MARCM experiments**

Wandering larvae were collected 48 hours after clone induction following a 37°C heat-shock of 8 or 10 minutes. Analyse of twin clones was performed on local projection of the wing disc after fixation and staining. Only disc with sufficiently sparse distribution of clones were used (to assign twins unambiguously). To extract clone position and size, each mitotic recombination figure (twin spot or single clone) was manually outlined on FIJI and then automatically segmented by applying a Gaussian blur followed by an automated thresholding (Intermode white method). The centroid of each mitotic recombination figure was obtained by summing the centres of each individual patch of cells composing the twin spot, pondered by their relative area compared to the total area of the twin clone. Thus, the centroid of each mitotic recombination figure was given by the following formula:

$$Centroid\ (x,y)_{mitotic\ figure} = \sum_{clone\ i} (Centroid\ (x,y)_{\ patch\ i}\ ).\frac{Area_{patch\ i}}{Total\ Area\ twin\ clone}$$

Averaged clone surface was estimated through the segmented surface of GFP or RFP clones (using the local projection around the apical place of cells). Estimation of the clone size in cell number was obtained a posteriori by segmenting 3 wing discs stained with E-cad (using Tissue analyser[34]) and DSRF to position landmarks, and by estimating the averaged apical cell area for each compartment. The average surface of clone for each compartment was then divided by the local averaged cell size to obtain an estimation of cell number per clone and to correct for effects driven by inhomogeneity of cell apical size throughout the disc.

**Spatial maps of wing discs (twin clones and GC3Ai).**

Positions of 36 landmarks were manually set on Z projections of wing discs using FIJI. Landmarks were positioned according to the pattern of DSRF revealed by immunostaining, along the veins, margin and folds of the wing pouch (**Figure 1supp C**). Two methods were used to characterise a spatial map of the tissue based on landmarks position. For the first one, landmarks were geometrically aligned within each genotype using the General Procrustes Analysis (GPA)[35] as implemented in R geomorph package[36] . GPA translates the set of landmarks of each wing disc to the same origin, scales them to size, and rotate them until the coordinates of corresponding points align as closely as possible. GPA allows to superimpose as closely as possible several wing discs, thus allowing to superimpose signal from many individuals (**Figure 1F,G**). For the second mapping method, 14 additional landmarks were added (landmarks 37 to 44) at the centre of segments defined by other landmarks (for example landmark 37 was set as the centre of segment defined by landmarks 21 and 22 – **Figure 1supp C**). The 44 landmarks were thus used to define polygons dividing the wing disc tissue into 40 compartments. With this later approach, clones and apoptotic bodies (defined by GC3Ai or cleaved DCP-1 figures) were assigned to a compartment according to the coordinates of the centre of mass of the clone/apoptotic body. In order to account for uncertainty in clone/apoptotic body localisation (e.g., because of clone movement between the time of induction and imaging), as well for uncertainty in landmark positioning (e.g., because of immunostaining variability or user error), clone assignment included consideration of an error margin. We used the *st_buffer* function implemented in the *sf* package of R software to add an error margin at a distance of 11.8 µm (40 pixels) around compartment margins (**Fig. 1suppD**). As a result, buffered boundaries of neighbour

compartments overlap within each other and a given position in the tissue could be assigned to belong to more than one compartment. This results in a smoothing of the spatial map allowing to account for uncertainty in cells and landmarks positions.

To analyse the spatial pattern of GC3Ai in discs at 72 h AEL, the anti DSRF staining could not be used to draw the landmarks because at this stage the DSRF patterning is not yet established. Instead we stained the wing disc for Ptc and Wg to detect AP and DV compartment and subdivide the wing disc in 4 quadrants.

**Adult wing shape and size analyses**

Crosses were done by placing 50-100 couples in egg laying cages with juice-agar plates and kept at 25 °C. Freshly hatched larva from the agar plates were transferred to *Drosophila* vials with fly food as described above at a density of 30 individuals / vial, and grown at 18 °C, 25 °C or 29 °C until emergence of adults. Flies were collected and stored in ethanol 70 ° at room temperature until dissection. Only left wings from females were taken, and mounted dorsal side up on a glass slide in a solution of 1:1 ethanol 80% and lactic acid 90%. Imaging was carried out on a ZEISS Discovery V8 stereomicroscope using a ZEISS Axiocam ICc 5 camera. All wings were imaged in the same orientation and with the same imaging parameters. For the experiments using Gal80ts (**Figure 4** and **4supp**), flies were crossed in cages supplied with agar petri dishes and allowed to lay eggs for ~ 6 h. Freshly hatched larva were transferred to regular vials at a density of 30 individuals / tube, and placed at 18 °C or 29 °C. Once arrived at the fluid pupal stage, individuals where switched temperature (from 18 °C to 29 °C and vice-versa). Upon hatching, flies were collected for wing dissection.

Wing measurements were done using a semi-automated procedure for estimating the positions 12 landmarks and 37 semi-landmarks along the wing outline and veins (**Figure 4suppA**). This was done using Wings4 software [19, 20] which fits a B-spline model to the wing from which the coordinates of landmarks and semi-landmarks are extracted. Wings4 outputs were examined using CPR software[20] which allows to screen for outliers and to generate a consolidated datasets of landmarks and wing areas.

Landmarks data were geometrically aligned within each experiment using the General Procrustes Analysis (GPA)[35] as implemented in R geomorph package[36]. GPA

translates all wing images to the same origin, scales them to unit-centroid size and rotate them until the coordinates of corresponding points align as closely as possible. Differences in landmarks coordinates resulting from the GPA represent shape differences between wings. Wing shape of each individual is characterized by the value of 96 variables, coming from the Procrustes transformation of x and y coordinates of the 48 landmarks and semi-landmarks. To reduce dimensionality of the data, wing shape variation was analysed by Principal Components Analysis as implemented in the function *plotTangentSpace* (now deprecated and replaced by *gm.prcomp*) of the R *geomorph* package. Visualisation of the wing shape variation among the principal component axes was done by comparing wing shape of the individual presenting the lowest value along the axis, with the individual presenting the highest value. To enable visualization of local growth differences in the adult wing upon apoptosis inhibition, we used the program Lory[37] to show one pattern of relative expansion or contraction that can transform mean shape of control genotype into mean shape of genotypes where apoptosis was inhibited.

**Estimation of clone size differences in an exponential growth regime**

Here we want to estimate the expected spatial differences of clone size in an exponential growth regime given the estimated spatial differences of apoptosis rate based on twin-clone analysis. For the sake of simplicity, we assume that division rate and apoptosis rate are constant over time.

*Estimation of the clone extinction probability*

Upon recombination, two daughter cells of different colours are generated and continue to grow, divide and die. After a given time $T$ (time of observation), there are four possible outcomes: we can recover the two daughter clones, a single colour clone, green or red (the other clone died before time $T$), and finally both clones disappeared before time $T$ (which cannot be measured experimentally). For this estimation, we assumed that all genotypes have the same proliferation and death rates.

$n(t)$ is the size (number of cells) of a clone at the time $t$, a stochastic process that follows the same probability function for every clone. For every clone, we have $n(0) = 1$ . The probability of clone disappearance before time $t$. *i.e.* the extinction probability, $p_0(t)$ is defined as

$$p_0(t) = P(n(t) = 0).$$

Experimental data gives access to the number of single clones $N_s$ and number of fully recovered twin clones $N_d$ that we observe at the time $T$. From this, we can estimate the probability of extinction at the observation time $T$, $p_0 = p_0(T)$.

The expected number of single clones is $N_s = 2p_0(1 - p_0)$

The expected number of fully recovered twin clones is $N_d = (1 - p_0)^2$

which gives the estimator of $p_0$,

*(1)* $\hat{p}_0 = \frac{q}{2-q}$

where $q = \frac{N_s}{N_s+N_d}$

*Estimation of the clone size and relationship with apoptosis and proliferation rate*

Let $\mu(t)$ be mean value of $n(t)$, clone size in number of cell at time t. In theory,

$$\mu(t) = p_0(t) \cdot 0 + p_1(t) \cdot 1 + \cdots + p_i(t) \cdot i + \cdots,$$

where $p_i(t)$ is a probability to observe a clone of size $i$ at the given time $t$, or $p_i(t) = P(n(t) = i)$ and $\sum p_i(t) = 1$ for all $t$. In order to estimate $\mu(t)$ from the observations we use:

$$\hat{\mu} = \frac{k_0}{N} \cdot 0 + \frac{k_1}{N} \cdot 1 + \cdots + \frac{k_i}{N} \cdot i + \cdots,$$

where $N$ is a total number of clones (including clones of size “0”), $k_i$ is a number of clones of size $i$, and $\sum k_i = N$.

However, since we cannot observe clones of size 0 we cannot measure $k_0$ nor $N$. We therefore use $p_0 = \frac{k_0}{N}$ (the probability of clone extinction, see above), and the total number of observed clones $N_{obs} = N - k_0$. From these two we can estimate $N = \frac{N_{obs}}{1-p_0}$. Hence, we estimate $\mu$ with

*(2)* $\hat{\mu} = (1 - \hat{p}_0)\left(\frac{k_1}{N_{obs}} \cdot 1 + \cdots + \frac{k_i}{N_{obs}} \cdot i + \cdots\right).$

Each clone we observe is a result of a stochastic birth-death process, that is fully described by its death rate, $a$, which is a probability of an individual cell to die per unit time and its birth rate, $b$, which is a probability of an individual cell to divide per unit

time. While the size of the clone at the given time, $n(t)$, is a stochastic process, the mean size $\mu(t)$ can be approximated by a deterministic process and is given by a simple exponential functions:

*(3)* $$\mu(t) = e^{(b-a)t}$$

Furthermore, the probability to be extinct at the time $t$ ($n(t) = 0$) can be expressed as followed[38]

*(4)* $$p_0(t) = \frac{a - ae^{-(b-a)t}}{b - ae^{-(b-a)t}}$$

*Estimating the apoptosis rate and proliferation rates for each compartment.*

From the twin clone data and the proportion of single clone (**Figure 2C**), the averaged clone size (**Figure 3A**) and *(1)* we can estimate $p_0$, and $\mu$ for each sub-compartment of the wing disc, that we then use to estimate parameters $a$ and $b$ (apoptosis and division rate). For the fixed $t$, based on *(3)* and *(4)* we have:

*(5)* $$b = \frac{\ln(\mu)}{t} + a$$

and

*(6)* $$p_0 = \frac{a - \frac{a}{\mu}}{b - \frac{a}{\mu}}$$

Hence

*(7)* $$a = \frac{\ln(\mu)}{t\left[\frac{1}{\mu} + \frac{\mu - 1}{\mu p_0} - 1\right]}$$

*Estimating the expected differences of clone size between compartment assuming constant proliferation rate*

We use the fixed value of a birth rate, $b = 0.0657$ (average of the estimated *b* from *(5)*), as a fixed value for every compartment. We look for a death rates $a$ for each compartment using the expression for $p_0(a)$ *(4)*.To the best of our knowledge it is not possible to express explicitly $a$ from the given formulation, so we use numerical approach to calculate it. We plot function of $p_0$ as $p_0(a)$ and look for the point of

intersection with the measured value $\hat{p}_0$. In this way we estimate value of $a$. Then we use $a$ and the fixed value of $b$ to predict $\mu$ *(6)*, that we then compared with the estimated value $\hat{\mu}$ from the experimental data *(2)* correcting for the non-observable disappeared clones (see **Figure 3B**). We overall found a good correlation between the estimated clone size and the prediction, (correlation coefficient $\rho = 0.6$ , **Figure 3D**) suggesting that the spatial difference in apoptosis are to a good approximation sufficient to explain the spatial differences in average clone size.

### Statistics

Data were not analysed blindly. No specific method was used to predetermine the number of samples. The definition of n and the number of samples is given in each figure and associated legend. Error bars are standard error of the mean (s.e.m.) or confidency interval 95%. p-values are calculated through t-test if the data passed normality test (Shapiro-Wilk test) (see legends).

## References


1. Fuchs, Y., and Steller, H. (2011). Programmed cell death in animal development and disease. Cell *147*, 742-758.
2. Toyama, Y., Peralta, X.G., Wells, A.R., Kiehart, D.P., and Edwards, G.S. (2008). Apoptotic force and tissue dynamics during Drosophila embryogenesis. Science *321*, 1683-1686.
3. Monier, B., Gettings, M., Gay, G., Mangeat, T., Schott, S., Guarner, A., and Suzanne, M. (2015). Apico-basal forces exerted by apoptotic cells drive epithelium folding. Nature *518*, 245-248.
4. Claveria, C., and Torres, M. (2016). Cell Competition: Mechanisms and Physiological Roles. Annu Rev Cell Dev Biol *32*, 411-439.
5. Boulan, L., and Leopold, P. (2021). What determines organ size during development and regeneration? Development *148*.
6. Vollmer, J., Casares, F., and Iber, D. (2017). Growth and size control during development. Open Biol *7*.
7. Hariharan, I.K. (2015). Organ Size Control: Lessons from Drosophila. Dev Cell *34*, 255-265.
8. Voss, A.K., and Strasser, A. (2020). The essentials of developmental apoptosis. F1000Res *9*.
9. Eder, D., Aegerter, C., and Basler, K. (2017). Forces controlling organ growth and size. Mech Dev *144*, 53-61.
10. Tripathi, B.K., and Irvine, K.D. (2022). The wing imaginal disc. Genetics.
11. Martin, F.A., Herrera, S.C., and Morata, G. (2009). Cell competition, growth and size control in the Drosophila wing imaginal disc. Development *136*, 3747-3756.
12. Diaz de la Loza, M.C., and Thompson, B.J. (2017). Forces shaping the Drosophila wing. Mech Dev *144*, 23-32.
13. Milan, M., Campuzano, S., and Garcia-Bellido, A. (1997). Developmental parameters of cell death in the wing disc of Drosophila. Proc Natl Acad Sci U S A *94*, 5691-5696.
14. de la Cova, C., Abril, M., Bellosta, P., Gallant, P., and Johnston, L.A. (2004). Drosophila myc regulates organ size by inducing cell competition. Cell *117*, 107-116.
15. Levayer, R., and Moreno, E. (2013). Mechanisms of cell competition: themes and variations. J Cell Biol *200*, 689-698.

16. Schott, S., Ambrosini, A., Barbaste, A., Benassayag, C., Gracia, M., Proag, A., Rayer, M., Monier, B., and Suzanne, M. (2017). A fluorescent toolkit for spatiotemporal tracking of apoptotic cells in living Drosophila tissues. Development *144*, 3840-3846.
17. Potter, C.J., Tasic, B., Russler, E.V., Liang, L., and Luo, L. (2010). The Q system: a repressible binary system for transgene expression, lineage tracing, and mosaic analysis. Cell *141*, 536-548.
18. Awasaki, T., Kao, C.F., Lee, Y.J., Yang, C.P., Huang, Y., Pfeiffer, B.D., Luan, H., Jing, X., Huang, Y.F., He, Y., et al. (2014). Making Drosophila lineage-restricted drivers via patterned recombination in neuroblasts. Nat Neurosci *17*, 631-637.
19. Houle, D., Mezey, J., Galpern, P., and Carter, A. (2003). Automated measurement of drosophila wings. Bmc Evol Biol *3*.
20. Houle, D., Van der Linde, K., and Marquez, E. (2014). Wings: Automated Capture of Drosophila Wing Shape v. 4.0.
21. Leevers, S.J., Weinkove, D., MacDougall, L.K., Hafen, E., and Waterfield, M.D. (1996). The Drosophila phosphoinositide 3-kinase Dp110 promotes cell growth. EMBO J *15*, 6584-6594.
22. Ghosh, S.M., Testa, N.D., and Shingleton, A.W. (2013). Temperature-size rule is mediated by thermal plasticity of critical size in Drosophila melanogaster. Proc Biol Sci *280*, 20130174.
23. McDonald, J.M.C., Ghosh, S.M., Gascoigne, S.J.L., and Shingleton, A.W. (2018). Plasticity Through Canalization: The Contrasting Effect of Temperature on Trait Size and Growth in Drosophila. Front Cell Dev Biol *6*, 156.
24. Diwanji, N., and Bergmann, A. (2019). Two Sides of the Same Coin - Compensatory Proliferation in Regeneration and Cancer. Adv Exp Med Biol *1167*, 65-85.
25. Haynie, J.L., and Bryant, P.J. (1977). The effects of X-rays on the proliferation dynamics of cells in the imaginal wing disc ofDrosophila melanogaster. Wilehm Roux Arch Dev Biol *183*, 85-100.
26. Huh, J.R., Guo, M., and Hay, B.A. (2004). Compensatory proliferation induced by cell death in the Drosophila wing disc requires activity of the apical cell death caspase Dronc in a nonapoptotic role. Curr Biol *14*, 1262-1266.
27. Perez-Garijo, A., Shlevkov, E., and Morata, G. (2009). The role of Dpp and Wg in compensatory proliferation and in the formation of hyperplastic overgrowths caused by apoptotic cells in the Drosophila wing disc. Development *136*, 1169-1177.
28. Ankawa, R., Goldberger, N., Yosefzon, Y., Koren, E., Yusupova, M., Rosner, D., Feldman, A., Baror-Sebban, S., Buganim, Y., Simon, D.J., et al. (2021). Apoptotic cells represent a dynamic stem cell niche governing proliferation and tissue regeneration. Dev Cell *56*, 1900-1916 e1905.
29. Kawaue, T., Yow, I., Le, A.P., Lou, Y., Loberas, M., Shagirov, M., Prost, J., Hiraiwa, T., Ladoux, B., and Toyama, Y. (2021). Mechanics defines the spatial pattern of compensatory proliferation. bioRxiv, 2021.2007.2004.451019.
30. Merino, M.M., Rhiner, C., Lopez-Gay, J.M., Buechel, D., Hauert, B., and Moreno, E. (2015). Elimination of unfit cells maintains tissue health and prolongs lifespan. Cell *160*, 461-476.
31. Crossman, S.H., Streichan, S.J., and Vincent, J.P. (2018). EGFR signaling coordinates patterning with cell survival during Drosophila epidermal development. PLoS Biol *16*, e3000027.
32. Schindelin, J., Arganda-Carreras, I., Frise, E., Kaynig, V., Longair, M., Pietzsch, T., Preibisch, S., Rueden, C., Saalfeld, S., Schmid, B., et al. (2012). Fiji: an open-source platform for biological-image analysis. Nat Methods *9*, 676-682.
33. Herbert, S., Valon, L., Mancini, L., Dray, N., Caldarelli, P., Gros, J., Esposito, E., Shorte, S.L., Bally-Cuif, L., Aulner, N., et al. (2021). LocalZProjector and DeProj: a toolbox for local 2D projection and accurate morphometrics of large 3D microscopy images. BMC Biol *19*, 136.
34. Etournay, R., Merkel, M., Popovic, M., Brandl, H., Dye, N.A., Aigouy, B., Salbreux, G., Eaton, S., and Julicher, F. (2016). TissueMiner: A multiscale analysis toolkit to quantify how cellular processes create tissue dynamics. Elife *5*.
35. Rohlf, F.J., and Slice, D. (1990). Extensions of the Procrustes Method for the Optimal Superimposition of Landmarks. Syst Zool *39*, 40-59.

36. Adams, D.C., and Otarola-Castillo, E. (2013). geomorph: an r package for the collection and analysis of geometric morphometric shape data. Methods Ecol Evol *4*, 393-399.
37. Marquez, E.J., Cabeen, R., Woods, R.P., and Houle, D. (2012). The Measurement of Local Variation in Shape. Evol Biol *39*, 419-439.
38. van Kampen, N.G. (2007). STOCHASTIC PROCESSES IN PHYSICS AND CHEMISTRY Third edition PREFACE TO THE THIRD EDITION. North-Holl Pers Libr, Xi-Xi.

# Figure 1

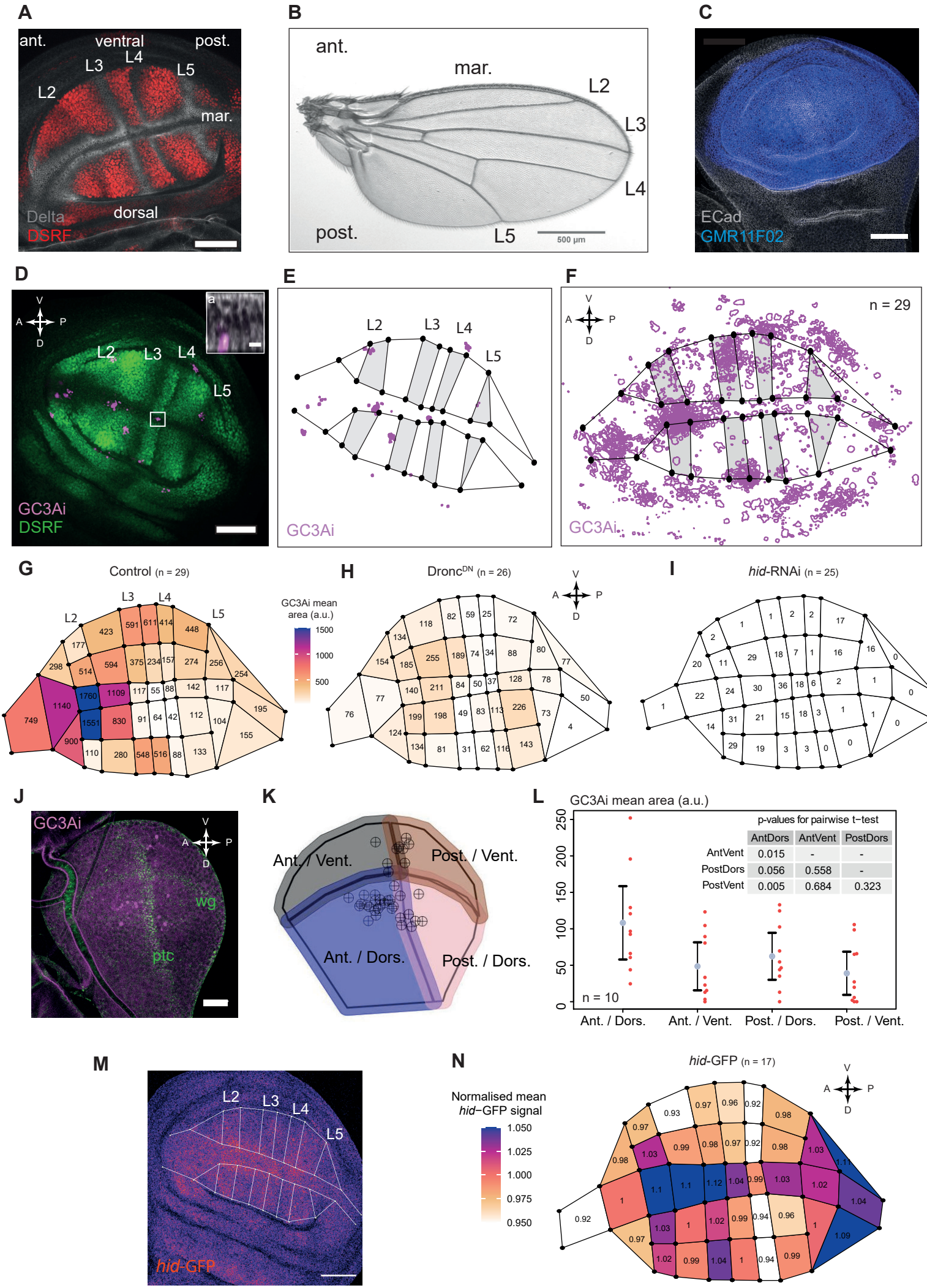
A
ant.
ventral
post.
L3
L4
L5
L2
mar.
Delta
DSRF
dorsal
B
ant.
mar.
L2
L3
L4
post.
L5
500 µm
C
ECad
GMR11F02
D
V
A
P
D
a
L2
L3
L4
L5
GC3Ai
DSRF
E
L2
L3
L4
L5
GC3Ai
F
V
A
P
D
n = 29
GC3Ai
G
Control (n = 29)
L2
L3
L4
L5
GC3Ai mean area (a.u.)
1500
1000
500
H
Dronc^DN (n = 26)
V
A
P
D
I
hid-RNAi (n = 25)
J
GC3Ai
V
A
P
D
wg
ptc
K
Ant. / Vent.
Post. / Vent.
Ant. / Dors.
Post. / Dors.
L
GC3Ai mean area (a.u.)
p-values for pairwise t−test
AntDors AntVent PostDors
AntVent 0.015 - -
PostDors 0.056 0.558 -
PostVent 0.005 0.684 0.323
n = 10
Ant. / Dors.
Ant. / Vent.
Post. / Dors.
Post. / Vent.
M
L2
L3
L4
L5
hid-GFP
N
hid-GFP (n = 17)
Normalised mean hid−GFP signal
1.050
1.025
1.000
0.975
0.950
V
A
P
D

**Figure 1: caspase-3 activity is spatially biased in the developing wing tissue.**

**A:** Wing disc at ~ 96 h after egg laying (AEL) showing veins (L2 to L5), interveins (red), dorsal, ventral, margin (mar.), anterior (ant.) and posterior (post.) territories. Red: anti-DSRF immunostaining. Grey: anti-Delta immunostaining. Orientation is the same for all wing discs images and schemes of this article, with the anterior compartment leftwards, and the dorsal compartment downwards. **B:** Female adult wing on dorsal view, with longitudinal veins (L2 to L5), margin (mar.), anterior (ant.) and posterior (post.) territories. **C:** Wing disc at ~ 96 h AEL showing the GMR11F02-GAL4 expression domain (blue). Gray: anti E-Cadherin immunostaining. **D:** z-projection of a wing disc showing caspase-3 activity using the GC3Ai reporter (magenta) expressed under the control of GMR11F02-GAL4 at ~ 96 h AEL. The inset is an orthogonal view of the white square, showing that the GC3Ai signal (magenta) points to apoptotic bodies located basally in the epithelium. a: apical. Grey: E-Cadherin. Inset scale bar: 5 µm. **E:** Segmentation output from the disc in **D**, showing the DSRF pattern and the GC3Ai segmented signal (magenta). Veins regions are gray. **F:** Superimposition of the segmentation data from 29 discs scaled, rotated and aligned using the General Procrustes Analysis (GPA), showing a spatially heterogeneous signal for GC3Ai (magenta). The map shown for vein / intervein territories is the average map from the 29 discs. **G-I:** Heat-maps showing the average GC3Ai positive area on each of the 40 compartments of the wing disc for the *control* (**G**, n = 29), *Dronc*$^{DN}$ (**H**, n = 26), *hid-RNAi* (**I**, n = 25) genotypes. Numbers within each compartment show the average value for GC3Ai positive area (arbitrary units). These values are also shown as a colour coded heat-map which has the same scale for three maps shown in G-I. **J:** Visualisation of caspase-3 activity using the GC3Ai reporter (magenta) expressed under the control of GMR11F02-GAL4 at ~ 72 h AEL. The wing disc is divided into four quadrants (Anterior-Dorsal; Anterior-Ventral; Posterior-Dorsal; Posterior-Ventral) using the immunostaining anti Wingless (wg) and anti Patched (ptc) marking compartment boundaries. **K:** Segmentation of the disc shown in **J**. The circled black crosses denote the centroids of the segmented GC3Ai signal. The black line was manually drawn using anti-Wingless and anti-Patched immunostainings to delineate the four quadrants, which are coloured. In order to account for uncertainty in centroid location and manual drawing of the contours, an overlap between the quadrants was allowed. **L:** Mean GC3Ai positive area for 10 discs at ~ 72 h AEL. One red dot represents one disc, blue circles are means and error bars are 95 % confidence intervals. The inset shows the p-values for all pairwise t-tests between quadrants. **M:** Pattern of *hid*$^{\Delta GFP}$(KI) on a single wing disc (LUT fire, Gaussian blur 0.75). White lines denote the vein/intervein territories extracted from the anti-DSRF immunostaining (not shown). **N:** Heat-map showing the mean *hid*$^{\Delta GFP}$ signal on each of the 40 compartments over n = 17 discs. To allow comparison of intensities among discs, the GFP signal intensity was normalised within each disc (i.e., within each disc, the value of each pixel was divided by the mean signal intensity over all the pixels of the disc). All scale bars are 50 µm length excepted in **B**, 500 µm, and in **J**, 25 µm.

# Figure 1 - supplement

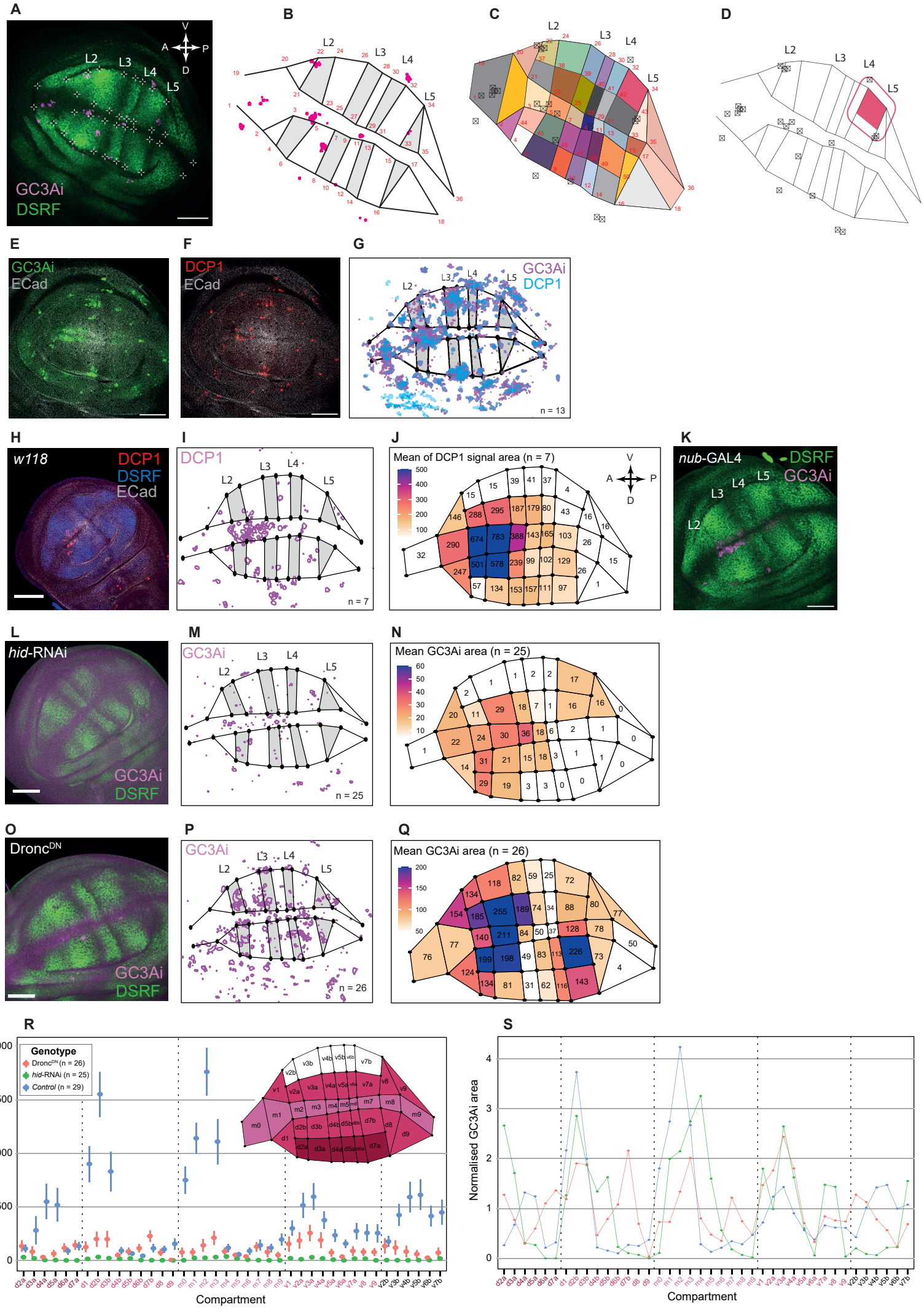

**Figure 1 –supplementary (related to Figure1)**

**A:** Wing disc from **Fig. 1-A** showing the 36 landmarks (white crosses) that were manually positioned at the intersections between veins (L2 to L5), folds and margin of the tissue, visible thanks to DSRF (green). **B:** Map of the wing disc shown in **A**, drawn from the landmark positions (black dots, numbered 1 to 36), and showing the segmented GC3Ai signal (magenta). Vein regions are in grey and intervein/margin regions in white. **C:** Division of the wing disc map shown in **B** into 40 compartments based on polygons (plain colours) defined with the landmarks. To this aim, 14 additional landmarks (numbered 37 to 50) were added at the middle of segments made by previously defined landmarks (see **Methods**). Boxed black crosses show the centroid of the GC3Ai segmented signal shown in B. **D:** Illustration of the error margin of the compartment boundaries used to account for uncertainty in signal localisation and landmark position. For each compartment, the margin was extended by 11.8 μm in order to encompass surrounding regions. In this example, the compartment defined by landmarks 32;34;43;42 (colored pink) has its margin extended and as a result the three GC3Ai centroids located around the compartment (boxed black crosses) will be considered as being also part of this compartment. **(E-G):** Co-localisation of GC3Ai and cleaved DCP-1 (*Drosophila* caspase3). **E** and **F** show the same wing disc with GC3Ai signal (**E**) or anti cleaved DCP-1 immunostaining (**F**). **G:** Superimposition of GC3Ai (magenta) and cleaved DCP-1 (blue) signals from 13 discs. The 13 discs were superimposed using the General Procrustes Alignment (GPA) based on the 36 landmarks positions. **H:** Wings disc from *w118* genotype stained for anti cleaved DCP-1, anti DSRF and anti E-cad. **I:** Superimposition of the segmentation data from 7 discs scaled, rotated and aligned using the GPA approach, showing a spatially heterogeneous signal for cleaved DCP-1 (magenta) in a similar pattern than the one for GC3Ai (**Fig. 1F,G**). **J:** Heat-map showing the average cleaved DCP-1 positive area on each of the 40 compartments of the wing disc in *w118* genetic background. Numbers within each compartment show the average value for cleaved DCP-1 positive area. These values are also shown as a colour coded heat-map. **K:** Wing disc stained with anti DSRF expressing GC3Ai under the control of *nubbin-GAL4*. **(L-N)**: Pattern of GC3Ai in *hid-RNAi* background driven by GMR11F02-GAL4, single representative wing disc (**L**), superimposition of 25 discs using GPA (**M**), and with a heat map showing the average GC3Ai signal area over 25 discs (**N**). **(O-Q)**: Pattern of GC3Ai in *UAS-Dronc$^{DN}$* background driven by GMR11F02-GAL4, single representative wing disc (**O**), superimposition of 26 discs using GPA (**P**), and heat map showing the average GC3Ai signal area over 26 discs (**Q**). **R:** Mean GC3Ai signal area for the 40 compartments in three genotypes (*Control*, *hid-RNAi*, *Dronc$^{DN}$*). The inset shows a wing disc diagram with delimitation and names of the 40 compartments on which the quantifications were made. Error bars show s.e.m. **S:** This plot shows the same data than in **R**, but that were normalised to show within each genotype how much the GC3Ai signal varies in a given compartment relatively to the average amount over all the disc. The plot was obtained by dividing the mean value of each compartment (shown in **R**) by the mean over all the compartment means within each genotype.

# Figure 2

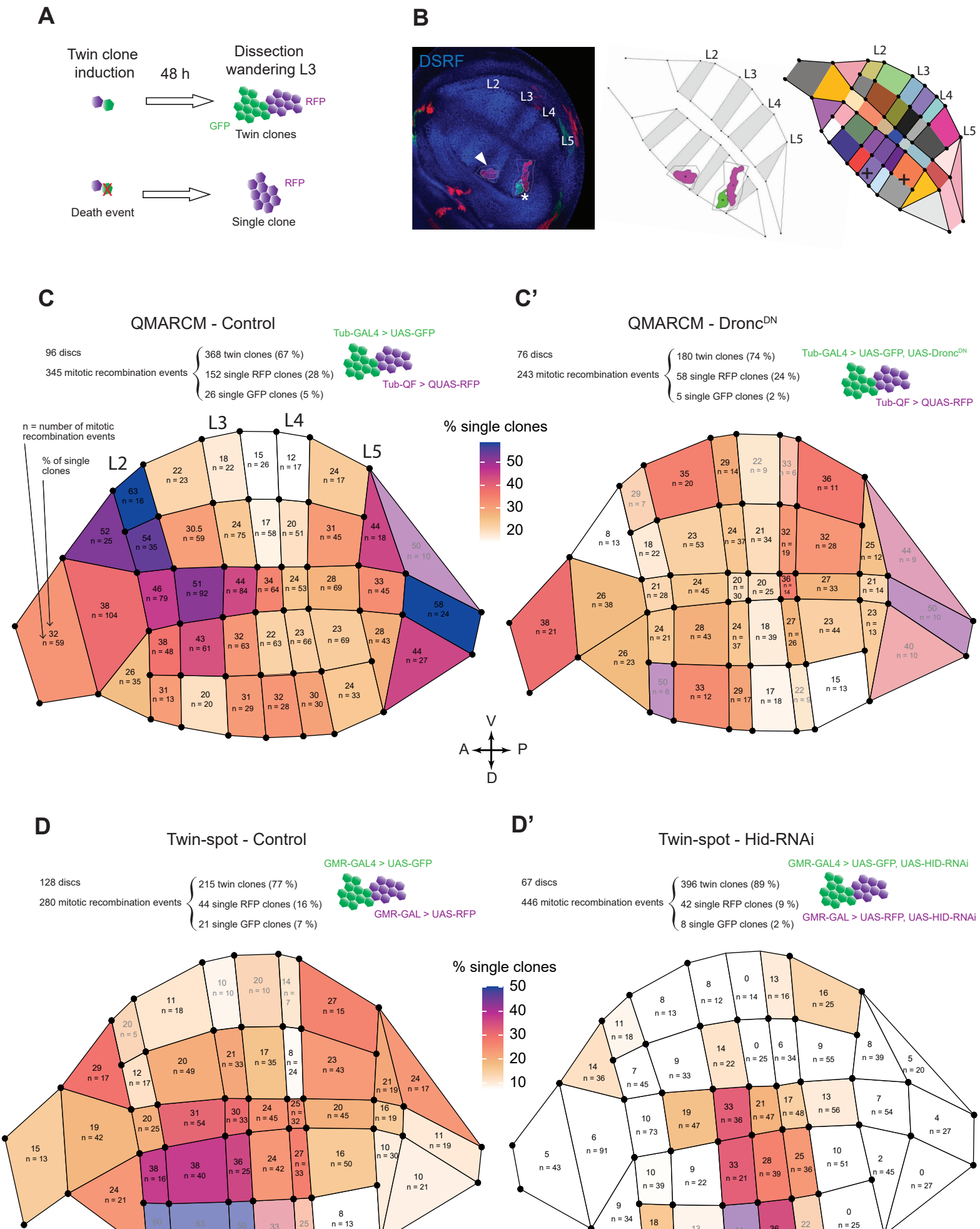
A
Twin clone induction
48 h
Dissection wandering L3
RFP
GFP
Twin clones
Death event
RFP
Single clone
B
DSRF
L2
L3
L4
L5
C
QMARCM - Control
96 discs
345 mitotic recombination events
368 twin clones (67 %)
152 single RFP clones (28 %)
26 single GFP clones (5 %)
Tub-GAL4 > UAS-GFP
Tub-QF > QUAS-RFP
n = number of mitotic recombination events
% of single clones
% single clones
50
40
30
20
C'
QMARCM - Dronc^DN
76 discs
243 mitotic recombination events
180 twin clones (74 %)
58 single RFP clones (24 %)
5 single GFP clones (2 %)
Tub-GAL4 > UAS-GFP, UAS-Dronc^DN
Tub-QF > QUAS-RFP
V
A
P
D
D
Twin-spot - Control
128 discs
280 mitotic recombination events
215 twin clones (77 %)
44 single RFP clones (16 %)
21 single GFP clones (7 %)
GMR-GAL4 > UAS-GFP
GMR-GAL > UAS-RFP
% single clones
50
40
30
20
10
D'
Twin-spot - Hid-RNAi
67 discs
446 mitotic recombination events
396 twin clones (89 %)
42 single RFP clones (9 %)
8 single GFP clones (2 %)
GMR-GAL4 > UAS-GFP, UAS-HID-RNAi
GMR-GAL > UAS-RFP, UAS-HID-RNAi

**Figure 2: clone disappearance is spatially patterned in the developing wing.**

**A:** Rationale for inferring cell death events from twin-clone induction experiments. Upon twin-clone induction and 48 h of growth, the observation of twin clones composed of one GFP and one RFP clone is expected. However, the occurrence of a cell death event upon clone induction will result in the occurrence of a single GFP or RFP clone without any twin counterpart in its vicinity. **B:** Spatial mapping for twin and single clone occurrences in the wing disc. Left, image of a wing disc at 96 h AEL stained with anti-DSRF and showing a single RFP clone (arrowhead) and a twin clone GFP-RFP (asterisk). Middle, manual segmentation of the tissue using the DSRF signal, and automated segmentation of the clones. Spatial map of the wing disc divided in 40 compartments (following the DSRF-based segmentation) into which clones positions are mapped. **C-D:** Spatial maps showing the pattern of single clone occurrences under different genetic conditions. In each case, the genotypes of the clones, the number of discs studied, the total number of mitotic recombination events, of twin clones, and of single clones observed are given. Colour scale of the heat maps show the % of single clones observed in each compartment, as a proportion of the total number of mitotic recombination events assigned to this compartment (n). For clarity, the compartments for which n ≤ 10 were shaded, since the inferred proportion from such low sample size are very unreliable. **C-C':** Spatial map of single clone occurrences obtained by inducing twin clones using the twin spot QMARCM system, in control conditions (C) and by additionally expressing UAS-Dronc$^{DN}$ in the GFP clone (C'). C and C' share the same colour scale. **D-D':** Spatial map of single clone occurrences obtained by inducing twin clones using the twin spot MARCM system driven by the GMR11F02-GAL4, in control conditions (D) and by additionally expressing UAS-HID-RNAi in all the pouch (D'). D and D' share the same colour scale.

# Figure 2 - supplementary

**A**

$$\text{Ratio} = \frac{(\text{area GFP clone}) - (\text{area RFP clone})}{(\text{area GFP clone}) + (\text{area RFP clone})}$$

## Case 1 : QMARCM - Control

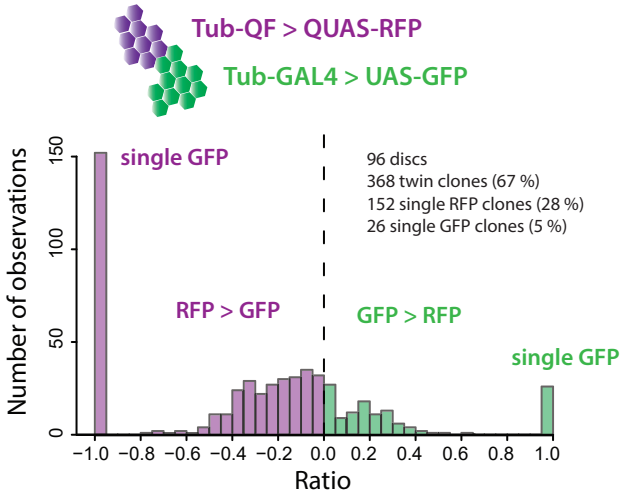


## Case 2 : QMARCM - Dronc$^{DN}$

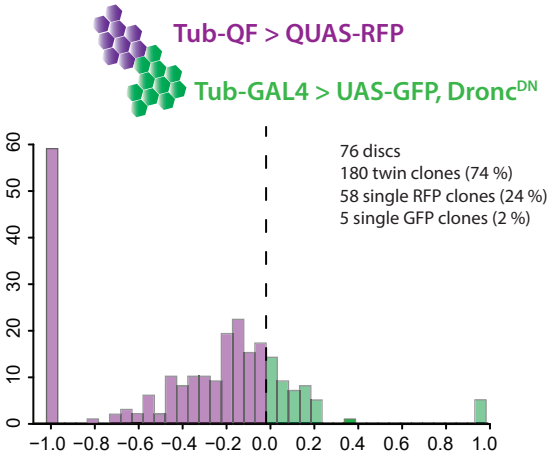


## Case 3 : MARCM - Control

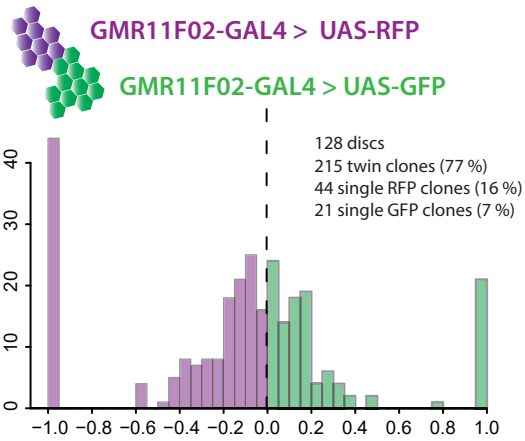


## Case 4 : MARCM - HID-RNAi

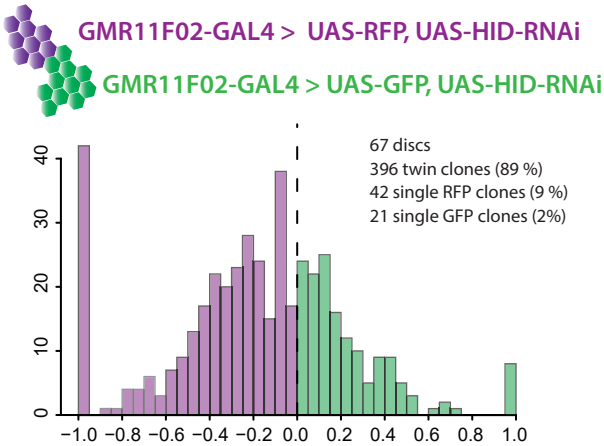


**B**

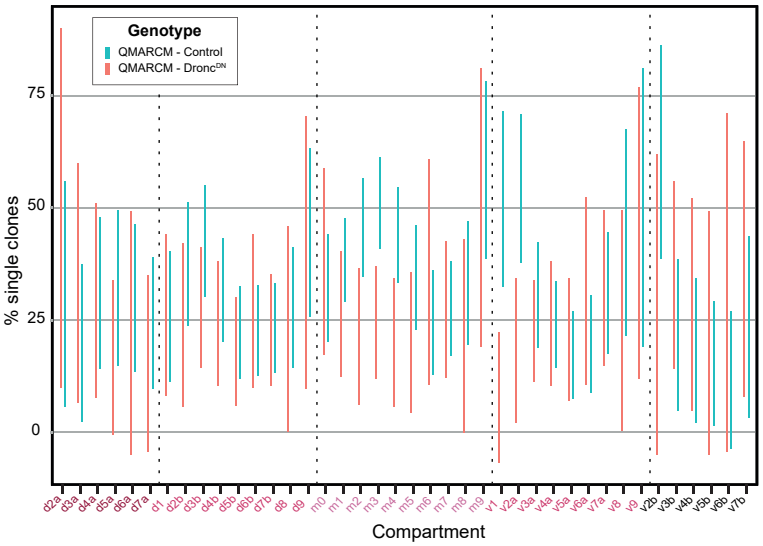


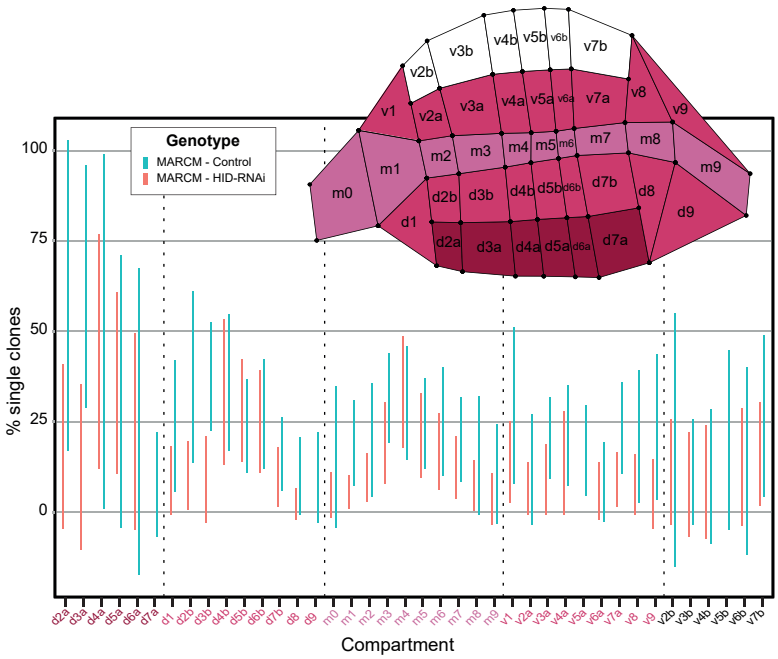

**Figure 2 – supplementary (related to Figure 2)**

**A:** Distribution of twin-clone Ratio values for each of the four genetic conditions studied to establish the spatial map of single clone occurrences. For each mitotic recombination event, the computed ratio is the difference between areas of the green and red clones over the sum of these areas. Negative ratios indicate twin clones for which the red clone is bigger than the green ones whereas twin clones where the green clone is bigger than the red one have positive values. Ratios values of -1 and +1 indicate mitotic recombination events where the green or the red clone were lost and have thus a null area. **B:** Frequency of the single colour clones for the 40 compartments in four genotypes (left, QMARCM, QMARCM Dronc$^{DN}$, right, twin spot MARCM, twin spot MARCM HID-RNAi). The inset shows a wing disc diagram with delimitation and names of the 40 compartments on which the quantifications were made. Error bars are 95% confidency interval.

# Figure 3

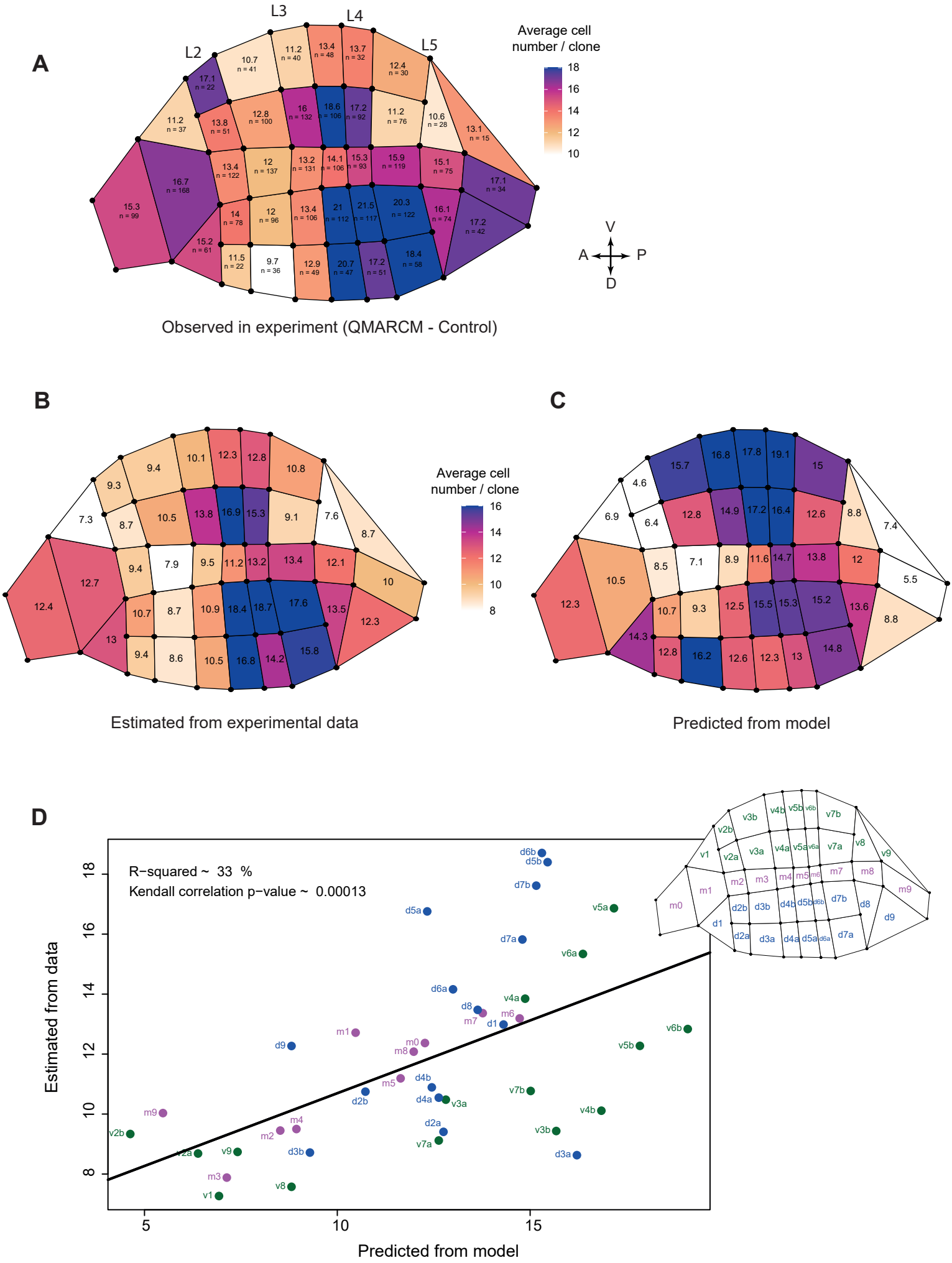
A
L2
L3
L4
L5
Average cell number / clone
18
16
14
12
10
V
A
P
D
Observed in experiment (QMARCM - Control)
B
Average cell number / clone
16
14
12
10
8
Estimated from experimental data
C
Predicted from model
D
R−squared ~ 33 %
Kendall correlation p−value ~ 0.00013
Estimated from data
Predicted from model
5
10
15
8
10
12
14
16
18

**Figure 3 – Local reduction of clone size can be predicted by the local upregulation of apoptosis.**

**A:** Spatial map for average cell number per clone in QMARCM – control experiment. Clones were considered irrespective of their colour. For each compartment, the average clone surface was calculated and divided a posteriori by the average cell apical size obtained in the same compartment to obtain an estimation of the averaged cell number per clone (see **Methods** and **Figure 3supp**). **B:** Spatial map of the mean value of clone size ($\mu(t)$, see **Methods**) which integrates the experimental average clone size as well as the 0 values (estimated from the proportion of singe colour clone, see **Methods**). **C**: Spatial map of the averaged predicted number of cell per clone assuming a constant and homogenous growth rate throughout the pouch and heterogeneous rate of apoptosis estimated from the local proportion of single coloured clone (see **Methods**). B and C share the same colour scale bar. **D:** Correlation between the average cell number per clone predicted from the model and estimated from experimental data for each compartment. The black line is the linear regression. The R-squared of the regression and the p-value of a correlation test (Kendall) are shown. Each dot is the data for one compartment, coloured and named according to the map shown on the right side of the plot (blue: dorsal compartments d1 to d9; magenta: margin compartments m0 to m9; green: ventral compartments v1 to v9).

# Figure 3 - supplementary

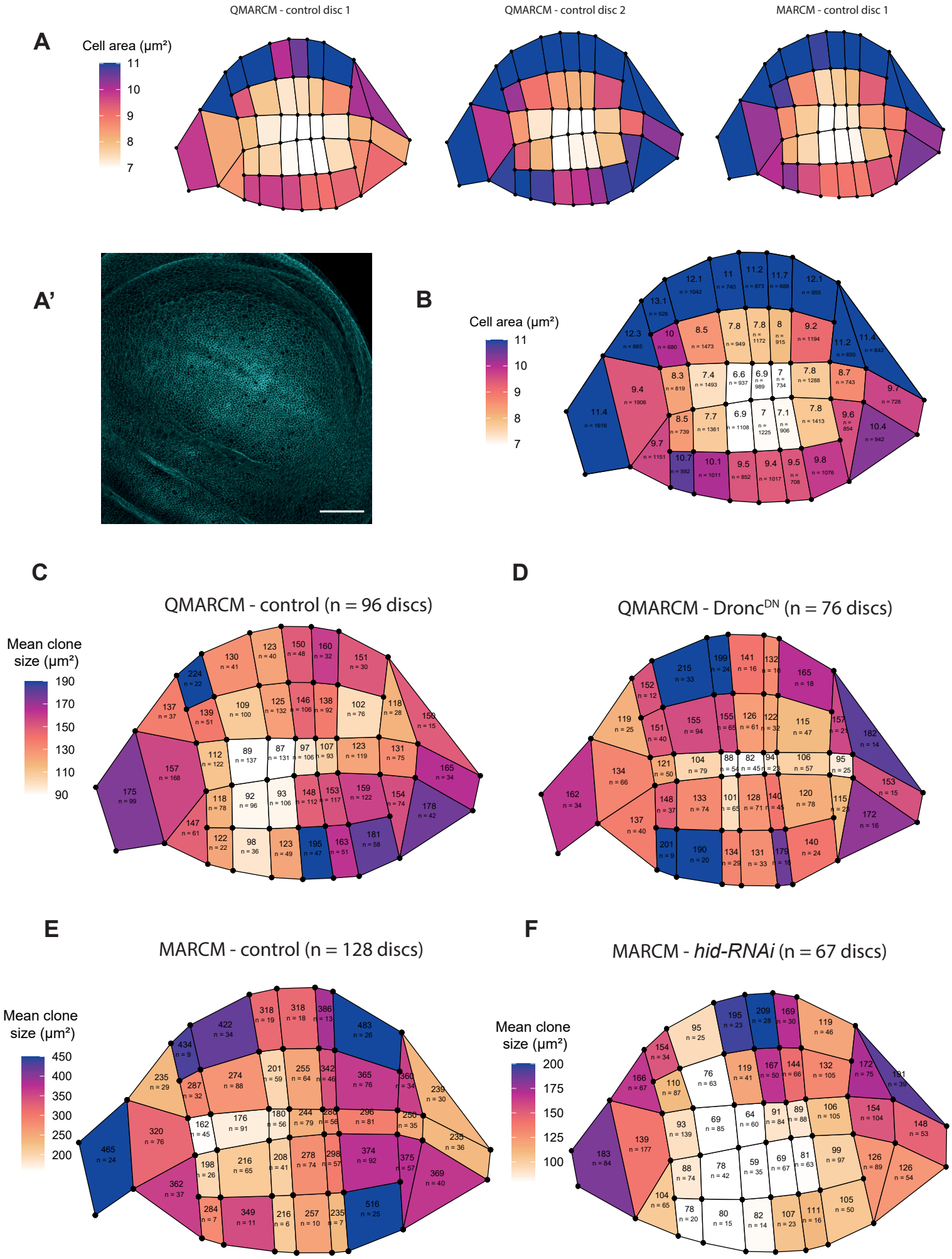

**Figure 3 – supplementary (associated with Figure 3)**

**A:** Heat maps showing the spatial pattern for cell apical area on three discs segmented. Two discs were of the *QMARCM – control* genotype and another one from the twin spot *MARCM – control* genotype. The colour code shows the averaged apical cell area for each compartment (same colour scale bar for the three disc). Overall, the three discs show very similar patterns of spatial variation of cell apical area. **A':** Example of a local projection of a wing disc stained with E-cad (the one shown in **A**). Scale bar : 50 µm. **B:** Heat map showing the average spatial pattern of cell size from the three discs shown in A. Within each compartment, the value for cell size (µm²) and the number of cells measured (over the three discs) are given. **C-F:** Heat maps showing the average spatial pattern for clone surface area (µm², based on local projections performed at the level of adherens junctions). Each clone was considered irrespectively of its colour and its occurrence as single clone or in a twin spot. For each compartment, the average surface area of the clones and the number of clones examined (n) are given. The data are shown for the four conditions examined in this study: QMARCM system, in control conditions (**C**) and upon expression of UAS-Dronc$^{DN}$ in the GFP clone (**D**); twin spot MARCM system driven by the GMR11F02-GAL4, in control conditions (**E**) and by additionally expressing UAS-*hid*-RNAi in all the pouch (**F**).

# Figure 4

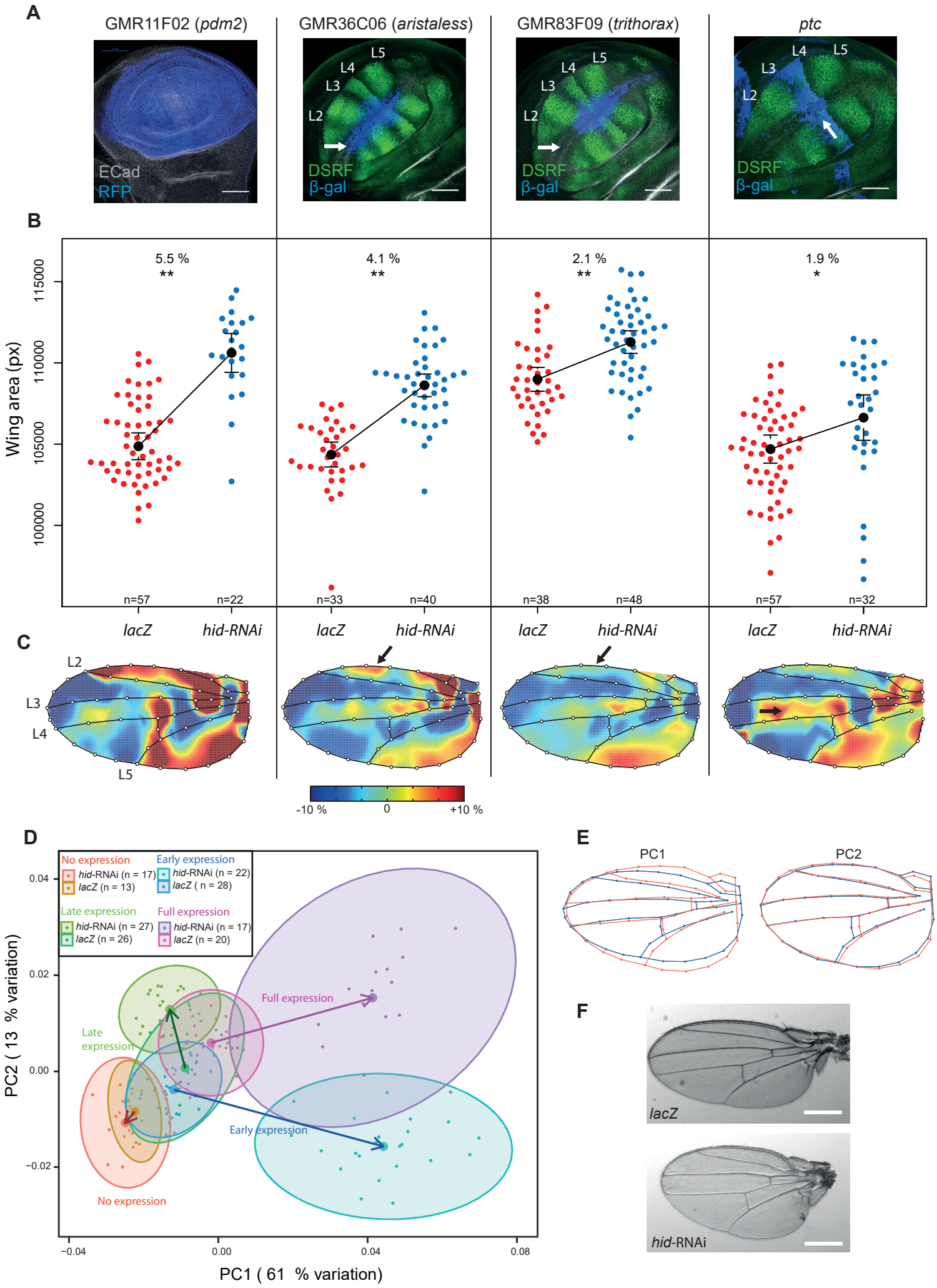
A
GMR11F02 (pdm2)
GMR36C06 (aristaless)
GMR83F09 (trithorax)
ptc
ECad
RFP
DSRF
β-gal
L2
L3
L4
L5
B
Wing area (px)
100000
105000
110000
115000
5.5 %
**
4.1 %
**
2.1 %
**
1.9 %
*
n=57
n=22
n=33
n=40
n=38
n=48
n=57
n=32
lacZ
hid-RNAi
C
-10 %
0
+10 %
D
No expression
hid-RNAi (n = 17)
lacZ (n = 13)
Early expression
hid-RNAi (n = 22)
lacZ ( n = 28)
Late expression
hid-RNAi (n = 27)
lacZ (n = 26)
Full expression
hid-RNAi (n = 17)
lacZ (n = 20)
Full expression
Late expression
Early expression
No expression
PC2 ( 13 % variation)
PC1 ( 61 % variation)
0.04
0.02
0.00
−0.02
−0.04
0.00
0.04
0.08
E
PC1
PC2
F
lacZ
hid-RNAi

**Figure 4: Apoptosis affects locally and globally wing size and shape during early stages of development.**

**A:** Pattern of expression at ~ 96 h AEL of the GAL4 drivers used to express *hid-RNAi*. White arrows show the most anterior region of the disc, where GAL4 is expressed in the case of *aristaless-GAL4*, but not in the case of *trithorax*-GAL4. **B:** Variation of adult wing size caused by expression of *hid*-RNAi under the control of different GAL4 drivers. For each GAL4 driver shown in **A**, the effect of expressing *hid*-RNAi compared to *lacZ* is shown. Each blue and red dot represents an individual wing size value, black dots are means, and error bars are 95 % confidence interval of the mean. For each driver, the % of variation of the *hid*-RNAi mean relative to the *lacZ* mean, as well as the results of pairwise t-tests between *lacZ* and *hid*-RNAi groups are shown. **: $p < 0.001$ ; * : $p < 0.01$. « n » denotes the number of wings for each group. **C:** Local variation of tissue shape caused by expressing *hid*-RNAi with different GAL4 drivers. Colours represent changes in relative area necessary to transform the average wing for *lacZ* group into the average wing of *hid*-RNAi group (number of wings shown in **B**). Colour bar shows the upper and lower limits in deformation. Highest colour intensity is reached at 10 % increase and decrease in local area in *hid*-RNAi group with respect to *lacZ* group. Arrows show the regions corresponding to the regions pointed by arrows in **A**. **D:** Principal components analysis (PCA) showing variation of wing shape (according to positions of 49 Procrustes-aligned landmarks and semi-landmarks) caused by expression of *hid*-RNAi at different developmental stages. Each small dot represents one wing shape. 8 conditions are shown (no expression, early expression, late expression and full expression of *hid*-RNAi or *lacZ* under the control of GMR11F02-GAL4). Big dots represent the mean of each condition. Vectors connect the mean of the *lacZ* group to the *hid*-RNAi group for each condition, thus allowing to visualise magnitude and direction of the effect on wing shape due to *hid*-RNAi expression. Ellipses are 95 % confidence intervals of the means. **E:** Diagrams showing the variation of wing shape along the first and the second principal component (PC) axes of the PCA shown in **A**, from low PC values (blue) to high values (red). **F:** Pictures of mounted wing illustrating the shape rounding observed upon *hid*-RNAi expression during early stages. Scale bars are 500 µm.

# Figure 4 - supplement

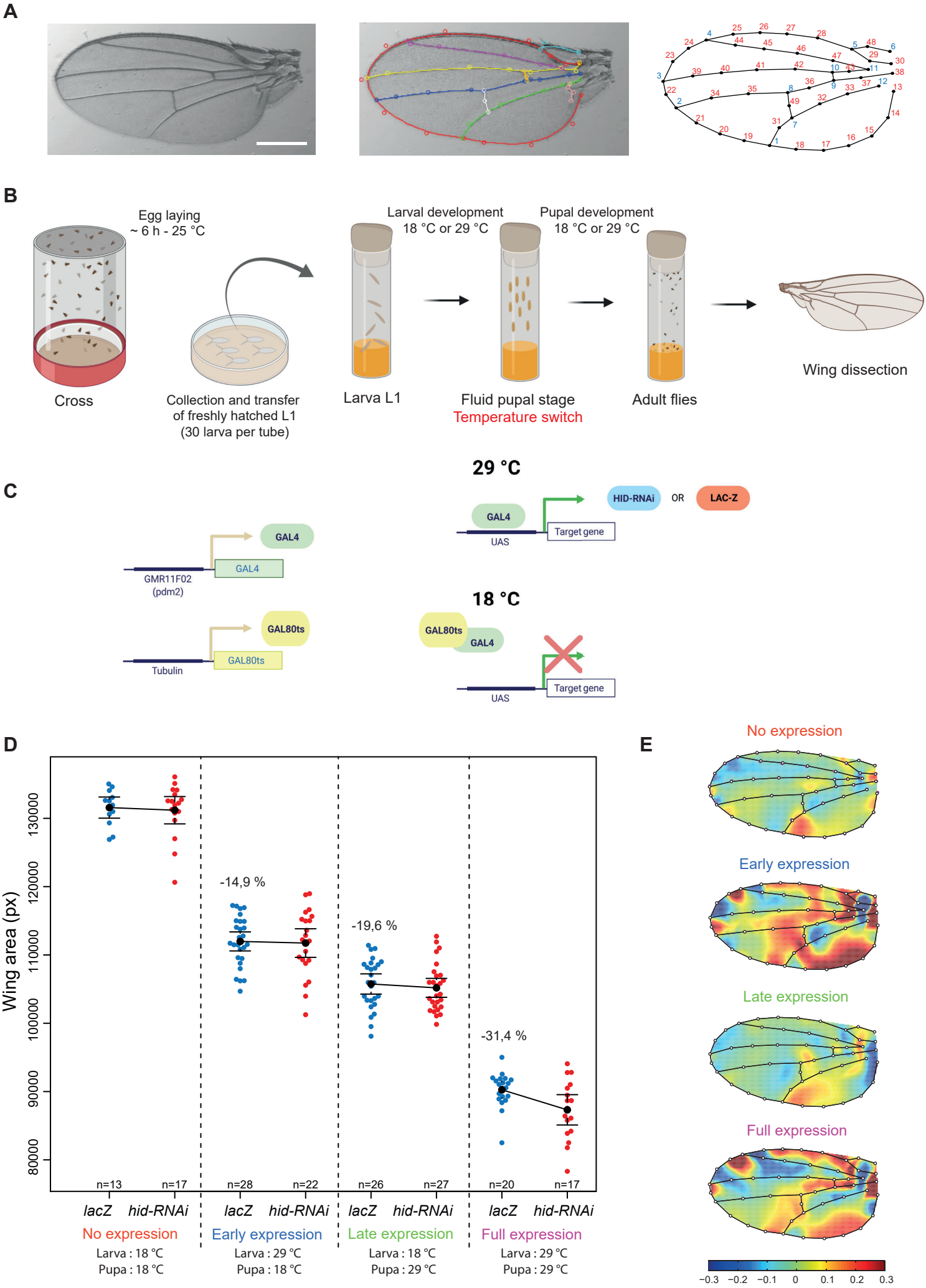

**Figure 4 – supplement (related to Figure 4)**

**A:** Adult wing segmentation pipeline. Left: wing example. Middle: the software Wings4 fits 9 spline curves (i.e., equations that give the location of the curve at any point between its end points) to veins and edges of the wing. Each spline is shown with a specific colour. Circles denote the positions of control points, which can be dragged manually by the user to maximise the overlap between the spline curves and veins and edges of the wing. Left: the program CPR extracts from the spline curves the positions of 12 landmarks (blue, numbered 1-12) and 36 semi-landmarks (red, numbered 13-48). Landmarks are strongly reliable points because they are located at the end of the curves. Semi-landmarks are less reliable because they are sampled along the curves by spacing them equally along each curve segment between each pair of landmarks. **B:** Experimental design for conditional gene expression during early or late developmental stages. Flies were crossed in cages supplied with agar petri dishes and allowed to lay eggs for ~ 6 h. Freshly hatched larva were transferred to regular vials at a density of 30 individuals / tube, and placed at 18 °C or 29 °C. Once arrived at the fluid pupal stage, individuals were switched temperature (from 18 °C to 29 °C and vice-versa). Upon hatching flies were collected for wing dissection. **C:** Rationale for conditional gene expression using tub-GAL80ts. GAL80ts has ubiquitous expression under the control of tubulin promoter whereas GAL4 expression is restricted to wing tissue under the control of GMR11F02-GAL4. At 18 °C, GAL80ts binds to the GAL4 and inhibits its activator function, precluding the expression of the target genes. At 29 °C Gal80ts is unable to bind GAL4, allowing GAL4 binding to the upstream activating sequence (UAS) and transcription of target genes (*lacZ* or *hid-RNAi*). **D:** Variation of adult wing size caused by expression of *hid*-RNAi under the control GMR11F02-GAL4 driver at different developmental stages. The effect of expressing *hid*-RNAi compared to *lacZ* is shown, for four conditions (No expression; Expression before fluid pupal stage (Early expression); Expression after fluid pupal stage (Late expression); Expression during all development (Full expression). Each blue and red dot represents an individual wing size value, black dots are means, and error bars are 95 % confidence interval of the mean. For each condition, the % of variation of the *lacZ* mean relative to the “No expression” condition is shown. Pairwise t-test for *lacZ* compared to *hid-RNAi* within each condition are all non-significant. **E:** Local variations of shape caused by expressing *hid*-RNAi at different developmental stages. Colours represent changes in relative area necessary to transform the average wing for *lacZ* group into the average wing of *hid*-RNAi group. Colour bar shows the upper and lower limits in deformation. Highest colour intensity is reached at 30 % increase and decrease in local area in *hid*-RNAi group with respect to *lacZ* group. Panels B and C were created with BioRender.com.